minerals

MDPI

Article

Cogenetic Origin of Magmatic Enclaves in Peralkaline Felsic Volcanic Rocks from the Sanshui Basin, South China

Peijia Chen [1,2], Bo Qian [1,*], Zhiwei Zhou [1] and Nianqiao Fang [2,*]

[1] School of Civil and Hydraulic Engineering, Xichang University, Xichang 615013, China; pjchen@xcc.edu.cn (P.C.)
[2] School of Ocean Science, China University of Geosciences, Beijing 100083, China
* Correspondence: qbydf@126.com (B.Q.); fangnq@cugb.edu.cn (N.F.)

Abstract: Centimeter-scale magmatic enclaves are abundant in peralkaline felsic volcanic rocks in the Sanshui Basin. Their lithology is mainly syenite and syenitic porphyry, and they mainly comprise alkali feldspar and amphibole, which is similar to the mineral assemblage of the host trachyte and comendite. The SiO_2 content in the syenitic enclaves is ~63 wt%, which is similar to that of the host trachyte but lower than that of the comendite. Thermobarometric calculations showed that the syenitic enclaves crystallized at similar temperature and pressure conditions as their host trachyte. The results of mass-balance modeling and MCS modeling indicate that the syenitic enclaves likely experienced an approximately 74% fractional crystallization from the basaltic parental magma. Combined with the similar mineral assemblages and geochemical characteristics of the host trachyte, we think that the enclaves resulted from the in situ crystallization of trachytic magma in the shallow crust and that they had a cogenetic origin with their host volcanic rocks, which means that they were likely to derived from the identical magma chamber which was formed from different batches of magma mixing/mingling. The recharge and mixing of basaltic magma triggered the eruption of trachytic magma eruption. The syenitic crust may have been disaggregated by the ascending trachytic magma and brought to the surface as syenitic enclaves. The syenitic enclaves in volcanic rocks provide unique information on the magmatism of the shallow crust as evidence of magma mixing/mingling.

Keywords: magmatic enclaves; peralkaline volcanic rocks; cogenetic; Sanshui Basin

Citation: Chen, P.; Qian, B.; Zhou, Z.; Fang, N. Cogenetic Origin of Magmatic Enclaves in Peralkaline Felsic Volcanic Rocks from the Sanshui Basin, South China. *Minerals* **2023**, *13*, 590. https://doi.org/10.3390/min13050590

Received: 22 March 2023
Revised: 21 April 2023
Accepted: 21 April 2023
Published: 24 April 2023

1. Introduction

Magmatic enclaves are widely recognized in both the plutonic and volcanic rocks [1]. Magmatic enclaves commonly found in calc-alkaline granites have been generically referred to as mafic microgranular enclaves (MMEs) to constrain the origin and evolution of the magma and crust-mantle interaction [2,3]. Although magmatic enclaves have been frequently studied, their origin is debated [2,4,5]. Their main sources include: (1) more mafic magma blobs mixed with felsic magma [1,2,6,7], (2) restitic enclaves formed by crustal remelting [8–10], (3) cumulated crystals of early minerals in the magma chamber [11–13], (4) rapidly cooling crystalline phases at the margins of magma conduits, and (5) trapped xenoliths [14,15]. The magma mixing/mingling model is the best model and indicates a crust–mantle interaction [4,6,16]. Fewer magma enclaves are present in volcanic rocks than in plutonic rocks; however, magmatic inclusions are also prevalent in some volcanic rocks [17–26], especially alkaline volcanic rocks [27–38]. Volcanic eruptions triggered by magmatism brought plutonic and subvolcanic samples to the surface, and these enclaves provide rich geological information and can study the deep earth [29,33,37]. The petrological, geochemical, and mineralogical characteristics of these enclaves provide unique information that can reveal the magmatic process of the shallow magma chamber.

For this study, the whole rock major, trace elements, and mineral chemistry of the syenitic enclaves commonly found in trachyte and comendite in the Sanshui Basin were investigated, whereby we conducted thermobarometric calculations and a thermodynamic model to explore the origin and petrogenesis of the syenitic enclaves, relationship with host trachyte and comendite, and constrained the magmatic process in the Sanshui Basin.

2. Geological Background

The Sanshui Basin is located at the margin of the South China Block (Figure 1a) and is constrained by the NE-trending Sihui–Wuchuan Fault, NW-trending Gangyao–Shawan Fault, and Xijiang Fault, and is shaped like a rhombus extending north-south with an area of approximately 3300 km^2 [39]. The basin is underlain by the Hercynian-Indosinian folded zone [40]. Because the area is influenced by the far-field effect of the subduction of the Paleo–Pacific and the Neo–Tethys plates [41], this region has been in an extensional setting and has formed the rift basin since the Late Cretaceous [42], and, ultimately, the continental lithosphere ruptured under the Sanshui Basin in the Cenozoic [43].

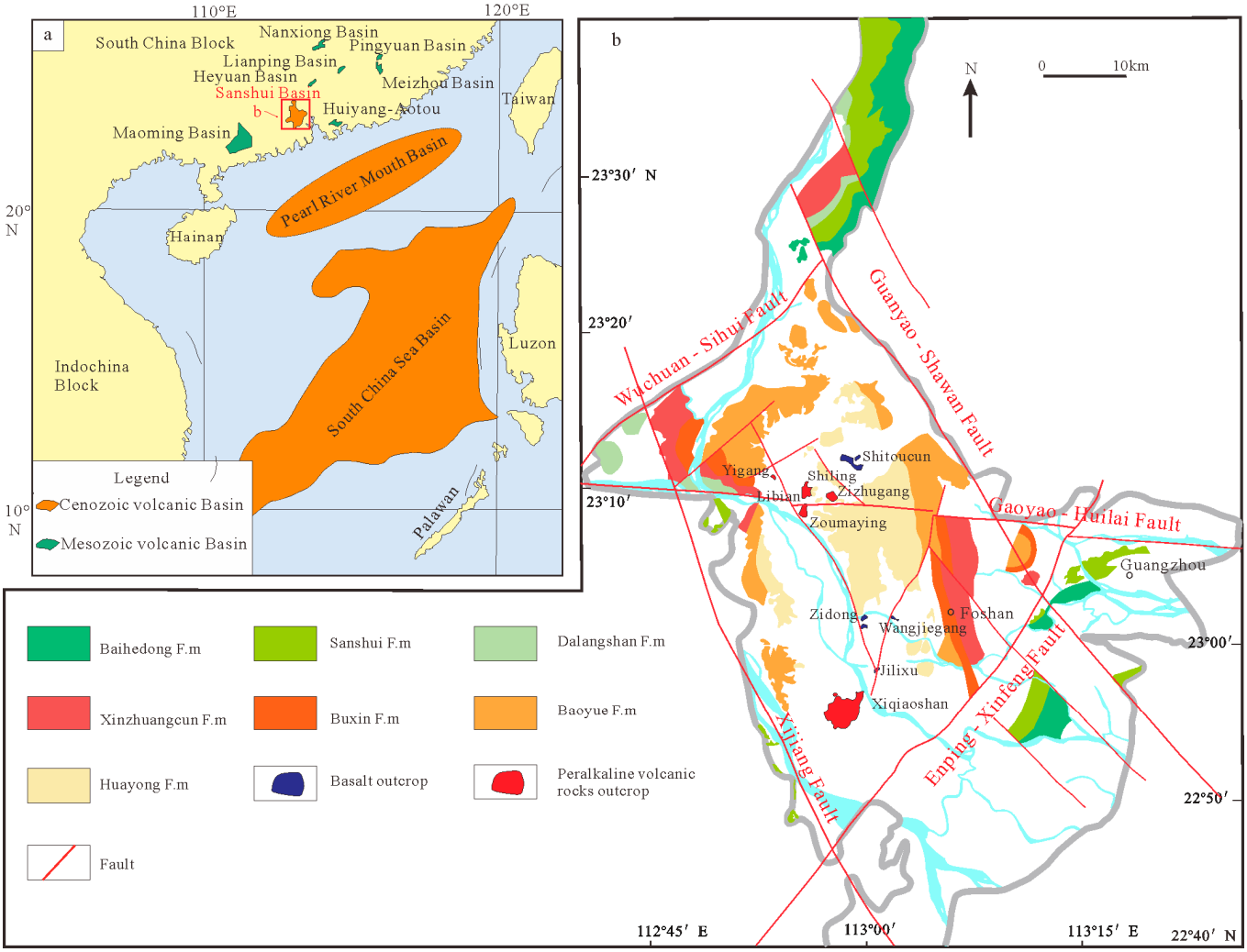

Figure 1. (**a**) Distribution map of volcanic basins in the northern continental margin of the South China Sea; (**b**) geological map of the Sanshui Basin.

From the Late Cretaceous to the Eocene (64–38 Ma), there were a total of 13 volcanic cycles and 123 eruptions occurred in the Sanshui Basin, and the thickness of the volcanic stratigraphy exceeded 2700 m [39]. These volcanic rocks are distributed in the center of the basin, with a north–south distribution of approximately 45 km and a bimodal volcanic assemblage dominated by trachyte and comendite in volume (whose total eruption thickness exceeds 1000 m and surface exposure area exceeds 14 km^2), followed by basaltic rocks. Based on the spatial distribution of trachyte and comendite, the Sanshui basin is divided into the Shiling cluster and the Xiqiao cluster (Figure 1b). The Cenozoic volcanic eruptions recorded in the Sanshui Basin occurred from 64 Ma to 38 Ma, but the main eruption period occurred from 53 Ma to 56 Ma [41]. The trachyte and comendite formed via protracted fractional crystallization (with insignificant crustal contamination) during the ascend of the basaltic magma into the crust [39,44].

3. Materials and Methods

We analyzed five syenitic enclaves collected from the Sanshui Basin, and our analysis included a major element and trace element analysis of the whole-rock and mineral chemical analysis.

The syenitic enclaves were crushed into approximately 200 mesh powders in an agate mill. The whole-rock major and trace element concentrations were obtained by using X−ray fluorescence (XRF) and inductively coupled plasma mass spectrometry (ICP−MS) at the ALS laboratory, Guangzhou. The major elements analyzed had analytical uncertainties of <5%. The trace elements were separated using cation-exchange techniques before running the ICP−MS analysis. The analytical uncertainties were estimated at 10% for the elements with abundances <10 ppm, and ~5% for those with abundance >10 ppm.

The mineral compositions in the syenitic enclaves were measured with a FE-EPMA (JEOL JXA-8530F Plus, Tokyo, Japan) equipped with five wavelength-dispersive spectrometers and an energy-dispersive spectrometer (EDS, OXFORD INSTRUMENTS X-MAX 20, Abingdon, UK) at the State Key Laboratory of Nuclear Resources and Environment, East China University of Technology, China. The accelerating voltage, beam current, and beam size were operated at 15 kV, 20 nA, and 1 μm, respectively. The peaks and backgrounds for P, Ti, Nb, Ta, Zr, Hf, U, Th, REEs, and Y were measured with counting times of 20 s and 10, and those for Si, Al, Mg, Ca, Mn, Fe, Na, and F were measured with counting times of 10 s and 5 s. All the data were corrected by using standard ZAF correction procedures. The analytical uncertainties were <1% for the major elements.

4. Results

4.1. Petrography

Syenitic enclaves are mainly found at Zoumaying, Libian (Figure 2b), and Zizhugang in the Shiling cluster and are generally between 1–5 cm in size. These enclaves are usually dark gray in color and thus have clear boundaries with a blue–green and purplish–red host rock. The magmatic enclaves exhibit a typical igneous texture and can be divided into medium-fine-grained syenite and syenite porphyry according to the texture; additionally, the main mineral assemblage is alkali feldspar and amphibole with minor clinopyroxene. alkali feldspar is the predominant mineral, up to 5 mm in size, with a transparent (fresh) –white color (altered), while amphibole is fine–grained and dark–green color.

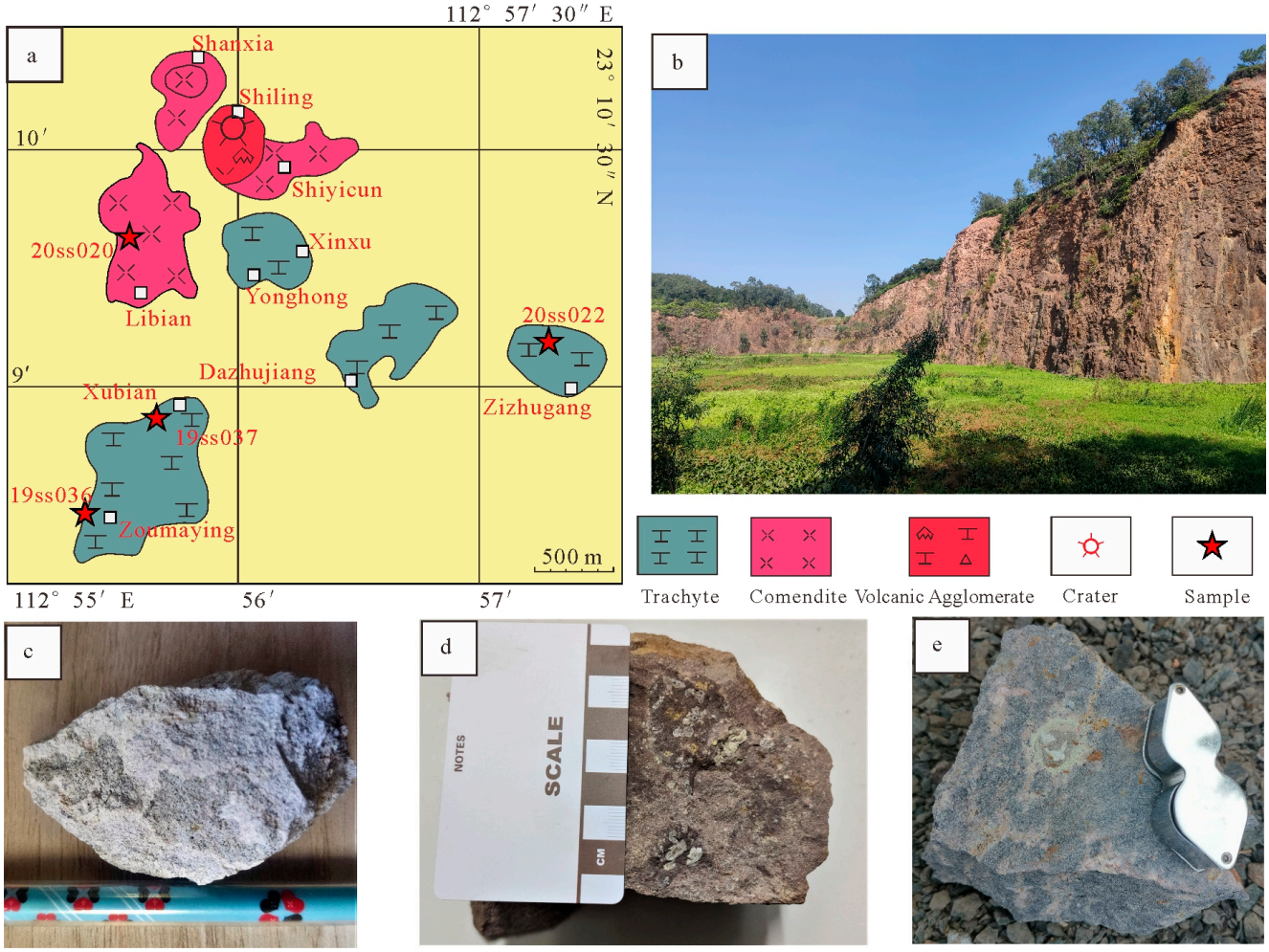

Figure 2. (**a**) Simplified geological map of the Shiling cluster; (**b**) oxidized comendite outcrop in Libian, Western Shiling; (**c**–**e**) hand specimen photographs of magmatic enclaves. Individual enclaves exhibit distinctive boundaries with host trachyte and comendite.

The medium-fine-grained syenite has a granular texture and consists of a large amount of alkali feldspar (>85 vol%) followed by minor amounts of sodium amphibole (4–8 vol%), clinopyroxene (<3 vol%), quartz (<3 vol%), and accessory minerals including Ti-Fe oxides, apatite, monazite, haleniusite, and zircon (Figure 3). The alkali feldspars phenocrysts are euhedral–subhedral with a slight alteration. The clinopyroxenes are subhedral–anhedral and are up to 7 mm in the 20ss022-1, whereas the sodium amphibole, quartz, and other accessory minerals are anhedral and filled in the alkali feldspar crystal framework.

The syenite porphyry has a porphyroid texture, and the phenocryst mineral is dominated by alkali feldspar, which is generally 3–7 mm in size and about 12 vol% in content. The groundmass minerals are dominated by microcrystalline alkali feldspar, Ti-Fe oxides, and sodium amphibole, with small amounts of apatite and zircon as accessory minerals.

The magmatic enclave host rocks are trachyte and comendite, both of the fresh host rocks are gray–green with a porphyritic structure, the phenocryst minerals are dominated by alkali feldspar, and the trachytes have 6–24 vol% phenocryst, whereas the comendites have 1–7 vol% phenocryst and are generally brick-red due to oxidation.

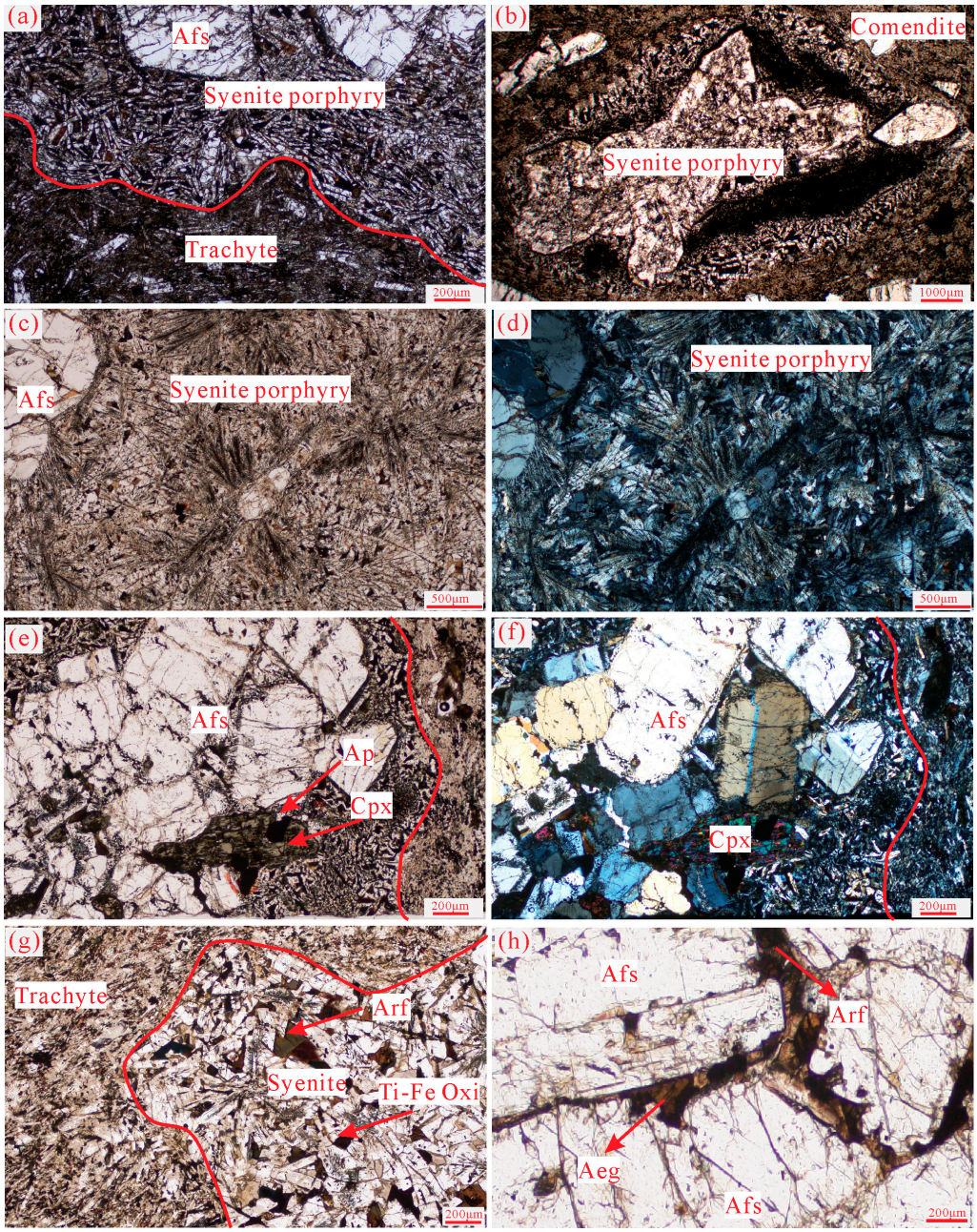

Figure 3. Representative photomicrographs of syenitic enclaves, individual enclaves exhibit distinctive boundaries with host trachyte and comendite. (**a**) the syenite porphyry and host trachyte, 19ss037-1, PPL; (**b**) the syenite porphyry and host comendite, the dark schlieren is mainly acicular amphibole, 20ss022-1, PPL; (**c**) the fibrous alkaline feldspar in syenite porphyry indicating high undercooling, 19ss036-1, PPL; (**d**) same field as (**c**), CPL; (**e**) the clinopyroxene in the syenite, the fine-grained alkali feldspar and amphibole indicating a rapid crystallization, 19ss022-1, PPL; (**f**) same field as (**e**), CPL; (**g**) anhedral amphibole fill in the alkali feldspar crystal framework in the sytnite, 14ss003-3, PPL, (**h**) anhedral aegirine fill in the alkali feldspar crystal framework in the sytnite, 19ss035-1, PPL. Afs, alkali feldspar; Cpx, clinopyroxene; Aeg, aegirine; Arf, arfvedsonite; Ap, apatite; Ti-Fe Oxi, Ti-Fe oxide. PPL = plane polarized light, CPL = crossed-polars light. The red line represents the boundary between the syenitic enclaves and the host rock.

4.2. Whole-Rock Geochemistry

The whole-rock geochemical composition of the syenitic enclaves are shown in Tables 1 and 2. The syenitic enclaves had a high loss on ignition (LOI, 1.03–1.71 wt%), and the high LOI may have been caused by the later alteration that resulted in low Na_2O content [45] which was also observed in the host rocks [41]. Therefore, the Na_2O concentration of syenitic enclaves was corrected using the method recommended by White [45]. A plot of FK/A vs. P.I. (FK/A = (Fe + K)/Al, mol, with all Fe calculated as Fe^{2+}, P.I. = (Na + K)/Al, mol) was presented in Figure 4a, enclaves from 19ss036-1 and 19ss037-1 lied below the 95% confidence interval and demonstrated the Na_2O loss. The Na_2O-corrected syenitic enclaves showed weakly peralkaline affinity with peralkaline index (P.I.) = 1.00–1.08.

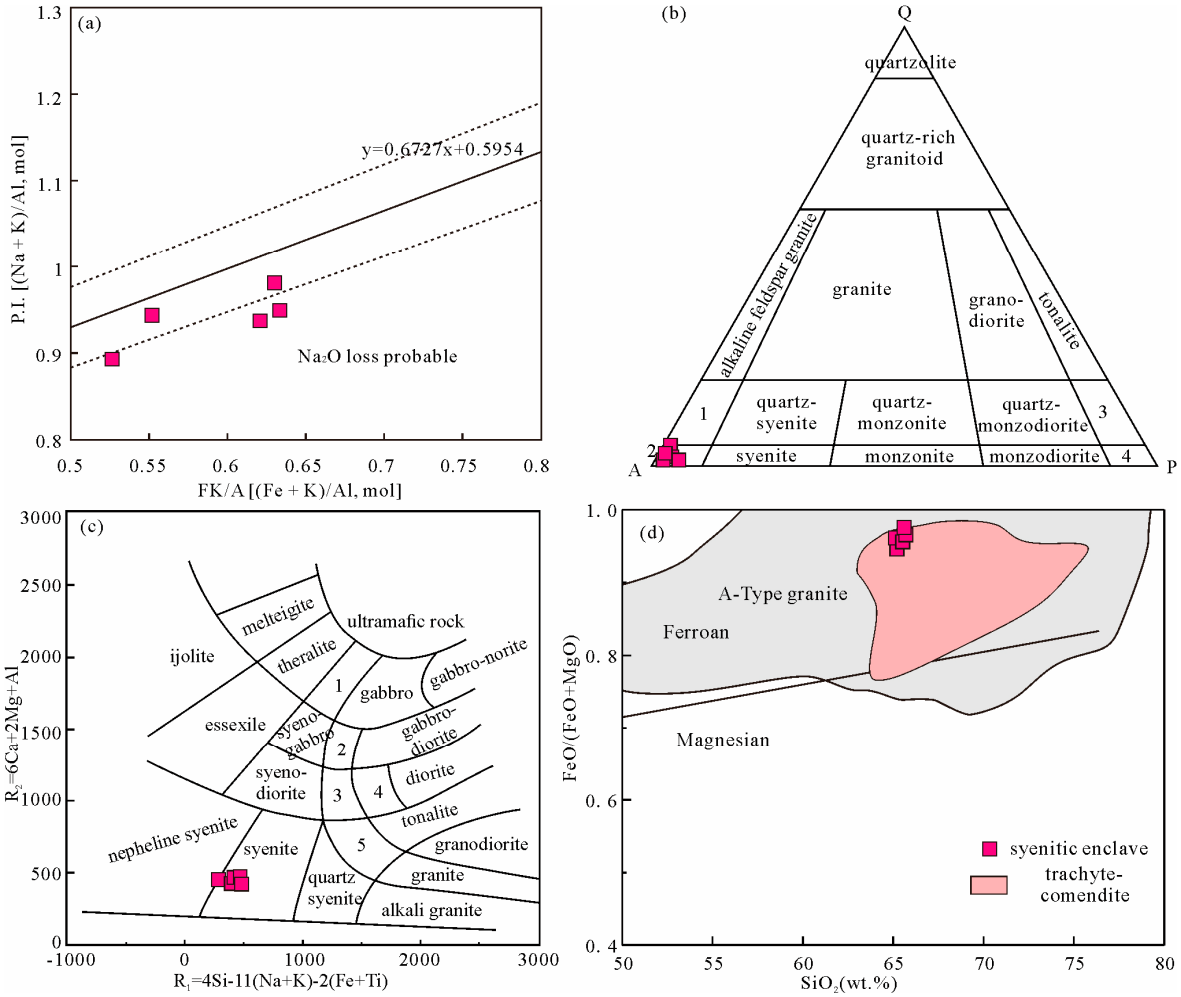

Figure 4. (**a**) FK/A vs. P.I diagram, after [45]. (**b**) QAPF diagram after [46]: 1, quartz alkaline feldspar syenite; 2, alkaline feldspar syenite, 3, quartz diorite; 4, diorite. (**c**) R_1 vs. R_2 classification diagram after [47]: 1, alkaline gabbro; 2, monzo-gabbro; 3, monzonite; 4, monzo−diorite; 5, quartz−monzonite. (**d**) SiO_2 vs. Fe/(FeO+MgO) diagram, after [48].

The major elements of the syenitic enclaves were similar to those of the trachyte exposed in the Sanshui Basin; they had high alkali content ($Na_2O^*+K_2O$ = 11.93–12.27 wt%), low MgO content (0.14–0.32 wt%), and low CaO (0.62–0.86 wt%), but the SiO_2 content was restricted (<1 wt% variation). All of the syenitic enclaves fell in the field of alkaline feldspar syenite field based on petrographic observation (Figure 4b) and plotted in the syenite field according to the classification (Figure 4c). The syenitic enclaves were ferroan with a

Fe/Fe+Mg value ranging 0.92 to 0.95, and alkaline with a MALI index (Na_2O+K_2O-CaO) range 11.40 to 11.61, corresponds to the A-type granite [48].

Table 1. Major elements composition of the syenitic enclaves of the Sanshui Basin.

Sample	19ss036-1	19ss037-2a	19ss037-2b	20ss020-1	20ss022-1	19ss036-1	20ss020-1	20ss022-1	Kilombe, Kenya	Azores, Portugal
Lat.(N)	23°8′43″	23°8′47″	23°8′47″	23°9′45″	23°9′10″	23°8′43″	23°9′45″	23°9′10″		
Lon.(E)	112°55′22″	112°55′47″	112°55′47″	112°55′41″	112°57′15″	112°55′22″	112°55′41″	112°57′15″		
rock type	syenite	syenite	syenite	syenite	syenite	trachyte	comendite	trachyte	syenite, n = 20	syenite, n = 17
group	enclave	enclave	enclave	enclave	enclave	host	host	host	enclave	enclave
SiO_2	63.84	63.58	63.19	63.77	63.26	64.51	71.74	65.47	62.10	62.77
TiO_2	0.49	0.46	0.47	0.44	0.51	0.36	0.42	0.31	0.64	0.62
Al_2O_3	17.03	15.77	16.11	16.56	16.10	15.66	12.51	15.55	15.72	16.89
FeOt	5.09	6.64	6.60	5.21	6.46	4.58	3.81	4.47	6.12	3.99
MnO	0.06	0.12	0.12	0.08	0.09	0.05	0.01	0.09	0.24	0.22
MgO	0.14	0.28	0.27	0.17	0.32	0.10	0.21	0.09	0.20	0.57
CaO	0.86	0.69	0.73	0.62	0.77	0.17	0.11	0.52	0.59	1.10
Na_2O	5.99	5.89	5.94	6.19	6.22	5.44	3.66	6.68	6.99	7.09
Na_2O*	7.06	7.13	7.23	6.92	7.15					
K_2O	4.94	4.87	4.91	5.02	5.13	5.37	5.16	5.41	5.32	5.29
P_2O_5	0.05	0.02	0.03	0.03	0.04	0.04	0.02	0.04	0.04	0.09
LOI	1.42	1.34	1.53	1.71	1.03	2.74	1.44	0.44	1.14	0.61
Total	99.91	99.66	99.90	99.80	99.93	99.02	99.09	99.07	99.11	99.23
P.I.	1.00	1.08	1.07	0.94	0.98					

The whole-rock chemical compositions of host rocks are from [41], Syenitic enclaves of Kilombe are from [34], and syenitic enclaves of Azores are from [29,30]. LOI: Loss on ignition. P.I. (Peralkaline Index) = Na+K/Al, mol.

Compared with the host rocks or other peralkaline felsic volcanic rocks in the Sanshui Basin, the variation of in the trace elements in the syenitic enclaves was restricted. The primitive mantle normalized pattern (Figure 5a) showed that all syenitic enclaves had enriched in high field strength elements (HFSE, such as Zr, Hf, Nb, and Ta) and were depleted in Ba, Sr, P, Eu, and Ti, which indicated the fractional crystallization of plagioclase, alkali feldspar, apatite, and Fe–Ti oxides during the magmatic evolution process, which was similar to what occurred with the host rocks. The chondrite normalized rare earth element pattern (Figure 5b) showed that the syenitic enclaves in the Sanshui Basin were characterized by moderate LREE enrichment relative to HREE, with $(La/Yb)_N$ ratios of 12.3–19.8, negative Eu anomalies (Eu/Eu* = 0.16–0.21) and various Ce anomalies (Ce/Ce* = 0.37–1.30), which was considered to be the result of hydrothermal alteration [41,49].

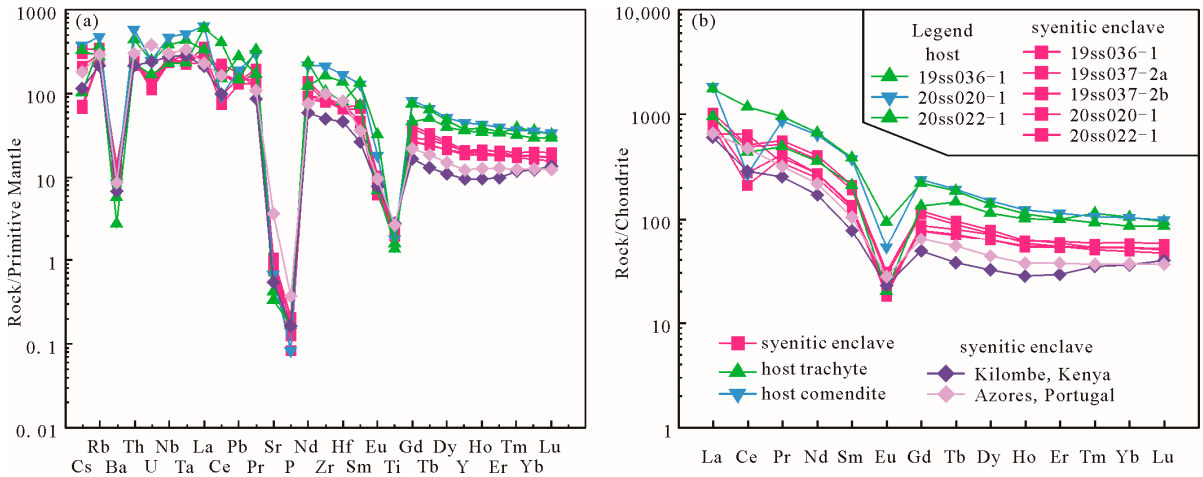

Figure 5. Primitive mantle normalized trace element distribution patterns (**a**) and chondrite normalized REE distribution patterns (**b**) for the syenitic enclaves in the Sanshui Basin. Syenitic enclaves of Kilombe are from [34], and syenitic enclaves of Azores are from [29,30]. Normalized values are from [50].

Table 2. Trace elements composition of the syenitic enclaves of the Sanshui Basin.

Sample	19ss036-1	19ss037-2a	19ss037-2b	20ss020-1	20ss022-1	19ss036-1	20ss020-1	20ss022-1	Kilombe, Kenya	Azores, Portugal
Rock Type	Syenite	Syenite	Syenite	Syenite	Syenite	Trachyte	Comendite	Trachyte	Syenite, n = 20	Syenite, n = 17
Group	Enclave	Enclave	Enclave	Enclave	Enclave	Host	Host	Host	Enclave	Enclave
Ba	98.00	65.20	75.60	88.10	72.30	40.90	61.10	19.70	48.70	61.00
Be	4.51	4.19	3.97	4.11	4.62	6.22	7.69	7.91		4.11
Co	0.60	1.00	1.00	0.80	0.90	21.40	0.30	0.60		4.16
Cr	1	1	1	1	1	1.3	3	2		
Cs	0.58	2.60	2.35	0.52	1.67	0.81	2.98	2.56	0.91	1.44
Ga	40.70	41.90	40.60	39.10	39.80	46.90	50.70	45.30	35.55	29.57
Hf	21.20	23.10	20.80	20.10	20.40	42.50	52.10	25.00	14.40	25.36
Nb	188	177	166	179	176	272	336	164	195	217
Ni	0.5	0.3	0.3	0.5	0.4	0.8	1.2	1.8		
Pb	10.00	9.20	12.40	9.30	10.80	19.50	13.60	10.40		
Rb	166	219	193	160	188	229	306	176	137	186
Sr	22.80	16.20	16.00	19.80	21.10	9.03	14.50	7.20	11.85	79.15
Ta	9.50	11.60	9.50	9.10	9.90	17.40	20.90	9.40	11.57	13.67
Th	19.35	22.30	21.40	18.20	23.30	36.90	49.50	19.45	18.31	25.64
U	3.25	2.74	2.33	3.01	2.45	5.16	5.20	3.54	5.03	7.97
V	17	5	6	14	8	1.33	2.0	1.0		35.75
Zr	972	997	883	903	913	1834	2360	1190	558	1119
Y	96	94	85	92	90	165	205	171	44	56
La	245	183	155	215	204	227	439	416	145	157
Ce	313	130	398	301	170	267	167	723	175	292
Pr	54	37	33	50	39	47	82	91	24	30
Nd	191	128	116	173	128	167	297	315	81	103
Sm	32.50	20.80	19.10	29.30	20.10	32.30	57.30	59.00	11.91	16.04
Eu	1.79	1.05	1.17	1.66	1.29	1.18	3.10	5.46	1.34	1.62
Gd	24.70	18.00	16.10	22.90	15.97	27.70	49.30	45.40	10.04	13.27
Tb	3.62	3.00	2.69	3.35	2.63	5.46	7.23	6.97	1.42	2.04
Dy	20.10	18.20	15.95	18.80	15.87	29.20	38.30	35.30	8.19	11.21
Ho	3.53	3.47	3.10	3.28	3.03	5.71	7.01	6.39	1.59	2.11
Er	9.66	10.05	8.98	8.91	8.77	16.50	19.00	16.80	4.82	6.21
Tm	1.35	1.48	1.34	1.28	1.37	2.92	2.72	2.38	0.89	0.94
Yb	8.88	9.99	9.02	8.21	8.94	17.80	17.60	14.65	6.15	6.27
Lu	1.28	1.47	1.31	1.18	1.30	2.42	2.52	2.20	1.02	0.93
La_N/Yb_N	19.79	13.10	12.33	18.78	16.37	9.15	17.89	20.37	16.89	17.99
Ce/Ce*	0.64	0.37	1.30	0.69	0.44	0.60	0.20	0.87	0.66	0.97
Eu/Eu*	0.19	0.16	0.20	0.19	0.21	0.12	0.17	0.31	0.36	0.33
Nb/U	58	64	71	59	72	53	65	46		

$Ce/Ce^* = 2Ce_N/(La_N + Pr_N)$, $Eu/Eu^* = 2Eu_N/(Sm_N + Gd_N)$, normalized from [50].

4.3. Mineral Geochemistry

We performed a mineral chemical analysis on the syenitic enclaves and the results are listed in the Tables 3–5.

Alkali feldspars were mainly classified as sanidine and anorthoclase (Figure 6a) with $An_{0–6}Ab_{53–74}Or_{22–44}$. The absence of an obvious zoned texture and the relatively stable composition of the alkali feldspars (Or variation < 5) indicated that they were in equilibrium with the host melt. The An content of alkali feldspars exhibited low (An = 0–6), and the Or values of the alkali feldspars in the syenitic enclaves hosted in the comendite varied more than in the trachyte (Table 3).

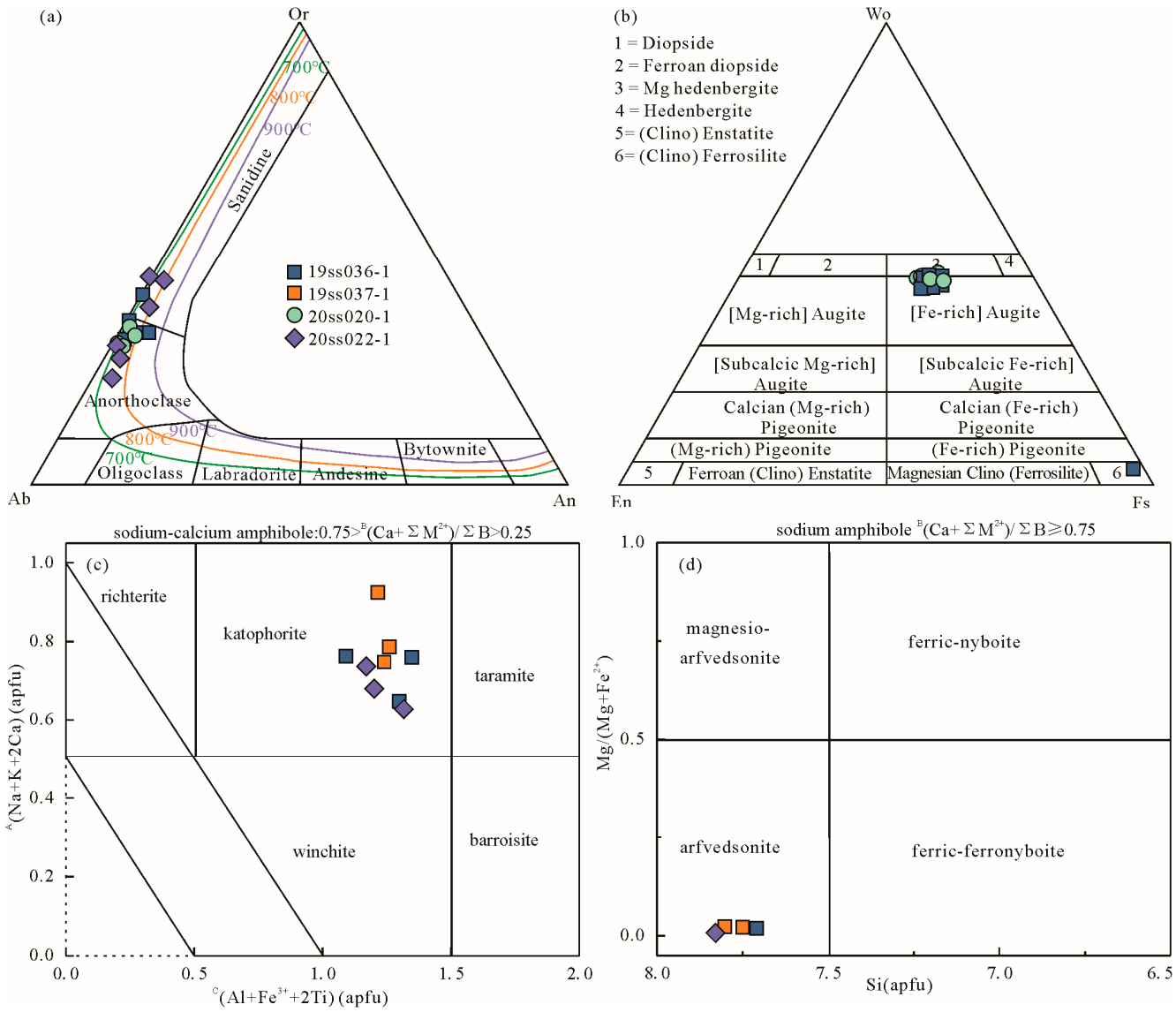

Figure 6. Mineral compositions of the syenitic enclaves. (**a**) Feldspar composition plotted into the ternary An-Ab-Or system, isotherm lines are from [51]; (**b**) clinopyroxene composition plotted into the Wo-En-Fs system after [52]; (**c**) sodium-calcium amphibole composition plotted in scheme diagram; (**d**) sodium amphibole composition plotted in scheme diagram after [53], $^{B}(Ca+\Sigma^{2+})$: Sum of Ca^{2+}, Fe^{2+}, and Mg^{2+} cations at B site in amphibole, ΣB: Sum of total cations at B site in amphibole.

Clinopyroxene was only observed in the enclaves (20ss022-1, 19ss036-1), and the clinopyroxenes were characterized by Mg# (Mg/Mg + Fe × 100) = 30–39 and a compositional range of $Wo_{43\text{-}45}En_{17\text{-}21}Fs_{34\text{-}39}$ with low Na contents (<0.45 apfu, atoms per formula unit), which was similar to the equilibrium clinopyroxenes in the host trachyte [57]. Aegirine observed in the alkaline feldspar framework (Figure 3h) had a composition of $Q_{18}Jd_{0}Aeg_{82}$, and Na apfu = 0.95.

According to the nomenclature of Hawthorne [53], amphiboles in the syenitic enclaves are classified as sodium-calcium and sodium amphiboles (Figure 6c,d) by using the machine learning method [58]. The amphiboles exhibited higher F concentrations (0.43–0.91 apfu) than the Cl concentrations (<0.021 apfu), and high $Fe^{2+}/(Fe^{2+} + Mg^{2+})$ ratios (0.97 to 0.99), which was similar to that of the amphiboles in A-type granite [59].

Table 3. Electron microprobe analyses of alkaline feldspar for the syenetic enclaves in the Sanshui Basin.

Point	036-2-1	036-2-2	036-2-3	036-2-4	036-2-5	022-2-1	022-2-2	022-2-3	022-2-4	020-2-1	020-2-2	020-2-3	020-2-4	020-2-5	020-2-6
SiO_2	66.77	67.49	66.95	65.87	66.60	67.76	67.27	68.40	65.36	66.83	66.46	66.83	67.81	67.69	66.95
TiO_2	0.05	0.02	0.02	0.05	0.03	0.06	0.04	0.02	0.07	0.04	0.11	0.00	0.05	0.13	0.06
Al_2O_3	18.47	18.57	18.82	18.87	19.32	18.49	18.74	17.70	18.84	19.60	18.70	17.84	18.16	18.49	17.84
FeOt	0.18	0.42	0.26	0.20	0.23	0.37	0.15	0.27	0.42	0.32	0.14	0.92	0.26	0.23	0.26
MnO	0.01	0.01	0.03	0.00	0.00	-	0.03	0.00	0.00	0.00	0.02	0.00	0.02	0.00	0.01
CaO	1.19	0.18	0.12	0.76	0.44	0.34	0.70	0.25	0.56	0.86	0.68	0.00	0.27	0.71	0.66
Na_2O	6.89	6.85	6.93	7.59	7.96	7.46	6.93	8.18	8.45	8.90	6.96	6.44	8.32	8.26	6.32
K_2O	5.49	5.67	7.27	5.82	5.60	5.89	5.16	5.45	5.55	4.13	6.80	7.84	5.42	4.81	7.88
Total	99.04	99.21	100.41	99.16	100.17	100.39	99.01	100.27	99.25	100.68	99.87	99.86	100.31	100.31	99.97
Formulae on basis of 8 oxygens															
Si	3.003	3.022	2.993	2.973	2.971	3.012	3.013	3.039	2.957	2.956	2.985	3.017	3.016	3.004	3.015
Ti	0.002	0.001	0.001	0.002	0.001	0.002	0.001	0.001	0.002	0.001	0.004	0.000	0.002	0.004	0.002
Al	0.979	0.984	0.992	1.004	1.016	0.969	0.989	0.927	1.004	1.022	0.990	0.949	0.952	0.967	0.947
Fe^{3+}	0.007	0.016	0.010	0.008	0.009	0.014	0.006	0.010	0.016	0.012	0.005	0.035	0.010	0.009	0.010
Mn	0.001	0.000	0.001	0.000	0.000	0.000	0.001	0.000	0.000	0.000	0.001	0.000	0.001	0.000	0.000
Ca	0.057	0.008	0.006	0.037	0.021	0.016	0.034	0.012	0.027	0.041	0.033	0.000	0.013	0.034	0.032
Na	0.600	0.598	0.600	0.665	0.688	0.643	0.602	0.705	0.741	0.764	0.606	0.563	0.718	0.711	0.552
K	0.315	0.325	0.414	0.335	0.319	0.334	0.295	0.309	0.320	0.233	0.389	0.451	0.307	0.272	0.453
total	4.964	4.955	5.017	5.022	5.024	4.990	4.940	5.003	5.068	5.028	5.014	5.015	5.018	5.000	5.011
An	6	1	1	4	2	2	4	1	3	4	3	0	1	3	3
Ab	62	64	59	64	67	65	65	69	68	74	59	56	69	70	53
Or	32	35	41	32	31	34	32	30	29	22	38	44	30	27	44
T	872	877	866	877	883	891	890	899	898	871	841	834	862	864	828

An = Ca/(Ca+Na+K) × 100, Ab = Na/(Ca+Na+K) × 100, Or = K/(Ca+Na+K) × 100. T = thermometeric calculations based on [54], T is in °C.

Table 4. Electron microprobe analyses of clinopyroxenes and thermobarometric calculations for the syenetic enclaves in the Sanshui Basin.

Piont	022-1	022-2	022-3	022-4	022-5	022-6	036-1	036-2	036-3	036-4	036-5	036-6	036-1
SiO_2	48.91	49.38	49.15	48.14	49.45	49.65	49.58	49.88	49.87	48.97	49.77	49.88	51.03
TiO_2	0.59	0.51	0.49	0.56	0.60	0.48	0.34	0.33	0.44	0.52	0.39	0.29	0.03
Al_2O_3	0.39	0.33	0.32	0.32	0.51	0.42	0.31	0.35	0.32	0.32	0.39	0.36	0.16
FeO	20.97	21.49	21.89	22.55	19.78	22.15	20.67	21.15	21.35	22.57	22.19	20.87	33.64
MnO	0.84	0.91	0.98	0.89	0.82	0.92	0.87	0.94	0.92	0.90	0.98	0.83	2.04
MgO	6.97	6.41	6.84	5.77	7.12	5.46	7.05	6.42	6.33	5.63	5.61	6.76	0.01
CaO	21.00	20.01	19.98	20.95	20.47	19.83	20.15	20.38	19.78	20.30	19.53	20.45	1.01
Na_2O	0.39	0.41	0.43	0.38	0.37	0.62	0.46	0.58	0.44	0.43	0.50	0.54	11.39
Total	100.05	99.45	100.08	99.56	99.14	99.52	99.44	100.03	99.44	99.64	99.36	99.97	99.31
Formulae on basis of 6 oxygens													
Si	1.945	1.972	1.956	1.942	1.967	1.985	1.973	1.977	1.986	1.965	1.991	1.976	2.121
Ti	0.018	0.015	0.015	0.017	0.018	0.014	0.010	0.010	0.013	0.016	0.012	0.009	0.001
Al	0.018	0.016	0.015	0.015	0.024	0.020	0.015	0.016	0.015	0.015	0.019	0.017	0.008
Fe^{3+}	0.129	0.063	0.115	0.143	0.052	0.043	0.081	0.079	0.030	0.083	0.022	0.084	0.922
Fe^{2+}	0.561	0.651	0.607	0.609	0.603	0.695	0.602	0.618	0.680	0.669	0.720	0.602	0.157
Mn	0.028	0.030	0.033	0.031	0.028	0.031	0.029	0.031	0.031	0.031	0.033	0.028	0.072
Mg	0.413	0.380	0.406	0.347	0.422	0.325	0.418	0.380	0.376	0.337	0.335	0.399	0.000
Ca	0.895	0.853	0.852	0.905	0.872	0.849	0.859	0.866	0.844	0.873	0.837	0.868	0.045
Na	0.030	0.032	0.033	0.030	0.029	0.048	0.036	0.044	0.034	0.033	0.038	0.042	0.917
Total	4.036	4.012	4.032	4.039	4.015	4.012	4.023	4.022	4.008	4.023	4.006	4.023	4.243
Wo	45	44	43	45	45	44	44	45	44	44	44	44	4
En	21	20	20	17	22	17	21	20	19	17	17	20	0
Fs	35	37	36	38	34	39	35	36	37	38	39	35	96
T1	-	-	-	-	-	880	-	-	898	-	880	-	-
P1	0.61	0.72	0.67	0.89	0.53	1.14	0.32	0.23	0.29	0.36	0.58	0.20	-
T2	867	869	867	867	888	867	869	867	875	867	870	883	-
P2	1.28	1.50	1.50	1.50	1.50	1.13	1.33	1.03	1.17	1.25	1.25	1.07	-
T3	936	938	935	925	940	925	877	875	875	867	869	876	-
P3	2	2	2	2	2	2	2	2	2	2	2	2	-

Wo = Ca/(Ca + Mg + Fe) × 100, En = Mg/(Ca + Mg + Fe) × 100, Fs = Fe/(Ca + Mg + Fe) × 100. T1 and P1= thermobarometric calculations based on cpx-melt model [55], T2 and P2 = thermobarometric calculations based on cpx-only model [56], T3 and P3 = thermobarometric calculations based on cpx-melt model [56], T is in °C and P is in kbar.

Table 5. Electron microprobe analyses of amphibole for the syenetic enclaves in the Sanshui Basin.

Point	022-1-1	022-1-2	022-1-3	022-1-4	036-1-1	036-1-2	036-1-3	036-1-4	037-1-1	037-1-2	037-1-3	037-1-4	037-1-5
SiO_2	49.75	50.38	48.93	49.63	49.96	49.25	48.27	49.72	48.67	48.88	49.50	50.14	49.08
TiO_2	0.30	0.94	1.01	0.67	0.78	1.13	0.60	0.70	0.47	0.65	0.74	0.64	0.76
Al_2O_3	0.19	0.39	0.49	0.56	0.33	0.49	0.37	0.53	0.54	0.62	0.45	0.46	0.59
FeOt	34.50	35.56	33.98	34.15	34.13	33.57	35.83	34.24	35.21	35.99	34.69	34.45	34.11
MnO	1.29	1.06	1.20	1.17	1.37	1.17	1.07	0.90	1.08	0.88	0.92	1.16	1.19
MgO	0.13	0.11	0.21	0.25	0.27	0.29	0.19	0.27	0.31	0.27	0.29	0.30	0.28
CaO	1.72	2.95	2.73	2.69	2.19	2.32	2.35	2.67	2.66	2.65	1.89	2.08	2.68
Na_2O	6.33	6.14	5.82	6.57	6.28	7.37	6.16	6.65	6.33	6.00	7.14	6.77	7.39
K_2O	1.32	1.30	1.34	1.37	1.33	1.37	1.33	1.34	1.33	1.30	1.35	1.36	1.36
F	2.05	1.33	1.43	1.39	1.67	1.21	0.98	2.15	1.90	1.69	1.59	1.76	1.92
Cl	0.03	0.05	0.03	0.09	0.06	0.05	0.02	0.05	0.04	0.07	0.06	0.05	0.07
Total	96.73	99.66	96.57	97.94	97.64	97.71	96.76	98.30	97.73	98.26	97.93	98.42	98.60
Formulae on basis of 23 oxygens													
Si	7.826	7.791	7.723	7.751	7.806	7.707	7.642	7.770	7.664	7.677	7.747	7.800	7.673
Al	0.137	0.150	0.237	0.197	0.147	0.235	0.325	0.176	0.299	0.283	0.199	0.146	0.274
Ti	0.011	0.045	0.023	0.038	0.027	0.048	0.016	0.037	0.015	0.022	0.041	0.036	0.037
T.sum	7.974	7.986	7.983	7.986	7.980	7.991	7.983	7.983	7.978	7.981	7.987	7.982	7.984
Al	0.000	0.000	0.000	0.000	0.000	0.000	0.000	0.000	0.000	0.000	0.000	0.000	0.000
Ti	0.024	0.064	0.097	0.041	0.065	0.085	0.056	0.045	0.041	0.055	0.046	0.039	0.052
Fe^{3+}	1.204	1.071	1.121	1.087	1.167	1.083	1.233	0.999	1.175	1.128	1.079	1.114	1.109
Mn^{2+}	0.144	0.124	0.136	0.137	0.153	0.140	0.122	0.107	0.124	0.101	0.111	0.134	0.141
Mg	0.029	0.026	0.050	0.058	0.064	0.069	0.044	0.064	0.073	0.063	0.068	0.070	0.065
Fe^{2+}	3.340	3.540	3.360	3.434	3.321	3.397	3.422	3.529	3.438	3.514	3.474	3.408	3.448
C.sum	4.741	4.826	4.764	4.758	4.769	4.774	4.877	4.743	4.852	4.861	4.778	4.764	4.816
Mn^{2+}	0.028	0.015	0.025	0.018	0.027	0.015	0.021	0.012	0.021	0.016	0.012	0.019	0.016
Fe^{2+}	0.000	0.000	0.005	0.000	0.000	0.000	0.088	0.000	0.024	0.084	0.000	0.000	0.000
Ca	0.444	0.600	0.603	0.579	0.501	0.524	0.551	0.579	0.589	0.582	0.461	0.478	0.578
Na	1.568	1.426	1.433	1.533	1.532	1.644	1.409	1.527	1.427	1.352	1.599	1.578	1.597
B.sum	2.040	2.041	2.065	2.130	2.060	2.183	2.069	2.118	2.060	2.034	2.072	2.074	2.192
Na	0.364	0.414	0.348	0.455	0.371	0.592	0.482	0.488	0.505	0.474	0.566	0.462	0.642
K	0.275	0.263	0.278	0.279	0.275	0.278	0.276	0.273	0.275	0.268	0.275	0.277	0.278
A.sum	0.639	0.678	0.626	0.735	0.646	0.871	0.758	0.761	0.780	0.742	0.841	0.739	0.919
F	0.912	0.587	0.636	0.618	0.739	0.543	0.434	0.972	0.855	0.758	0.714	0.782	0.869
Cl	0.007	0.013	0.007	0.021	0.016	0.012	0.005	0.013	0.010	0.017	0.014	0.013	0.018
Name	Arf	Ktp	Ktp	Ktp	Ktp	Arf	Ktp	Ktp	Ktp	Ktp	Arf	Arf	Ktp

T.sum, C.sum, B.sum, A.sum are the sum of cation at T site, C site, B site, and A site, respectively. Arf = Arfvedsonite, Ktp = Katophorite.

4.4. Thermobarometeric Calculation

To estimate the syenitic enclaves' crystallization condition and magmatic evolution, we performed a series of thermobarometric calculations on the syenitic enclaves to determine the magma crystallization condition.

The crystallization temperature of the syenitic enclaves was estimated by using clinopyroxene (cpx)-melt [55,56], cpx-only [56], and alkaline feldspar-melt [54] thermometers. When calculating the values obtained from the cpx-melt thermometer, we used an initial H_2O content of 4.5 wt% and pressure of 1.5 kbar, and the calculation results showed that the crystallization temperature ranged from 880 °C to 897 °C. The cpx-melt and cpx-only thermometers, which were based on random-forest machine learning, did not need additional conditions in the calculation [56]; the cpx-only thermometer provided a consistent estimate of 867–888 °C, and cpx-melt thermometer results showed crystallization temperatures ranging 867 °C to 877 °C for 19ss036-1 and exceeding 925 °C for 20ss022-1, which may have been related to the variations of melt composition. Similar results were calculated when using the alkaline feldspar-melt thermometer, with temperatures ranging 872 °C to 883 °C in 19ss036-1, 891 °C to 898 °C in 20ss022-1, and 828 °C to 871 °C in 20ss020-1.

The pressure of the syenitic enclaves were estimated by using cpx-melt [55,56] and cpx-only [56] barometer; the cpx-melt barometric calculations showed crystallization pressures ranged 0.17 to 1.14 kbar, the cpx-only barometric calculations showed a higher pressure of 1.07–1.50 kbar, and the cpx-melt barometer provided an estimate of 2 kbar. The thermobarometric results showed that, assuming a pressure to depth conversion of 2.8 km/kbar,

syenitic enclaves crystallized in the shallow crust which were similar to the results of the volcanic rock calculations [57].

5. Discussion

5.1. Geochemical Characterization of the Syenitic Enclaves

The syenitic enclaves in the peralkaline volcanic rocks were ferroan and alkaline, corresponded to the A-type granite [48]; these rocks mainly formed in an extensional tectonic setting [60]. On the Th/Ta vs. Yb diagrams [61], the syenitic enclaves fell in the intraplate volcanic rock field (Figure 7a), which is consistent with the tectonic context of the bimodal volcanic rocks [39,43]. The Rb vs. Ta + Yb [62], $(Th/Ta)_N$ vs. $(Y/Nb)_N$ [63], and Zr vs. 10,000 Ga/Al [60] diagrams indicated that they formed in an intraplate setting similar to the host trachyte and comendite. The Nb/Y vs. Nb + Y diagram [64] and the Nb-Y-3Ga ternary diagram [60] were clustered in the A_1-type rhyolite field, which indicated that they developed in a continental rift tectonic setting. The high FeO and low Al_2O_3 content in the amphibole also indicated that they formed in anorogenic tectonic setting [65].

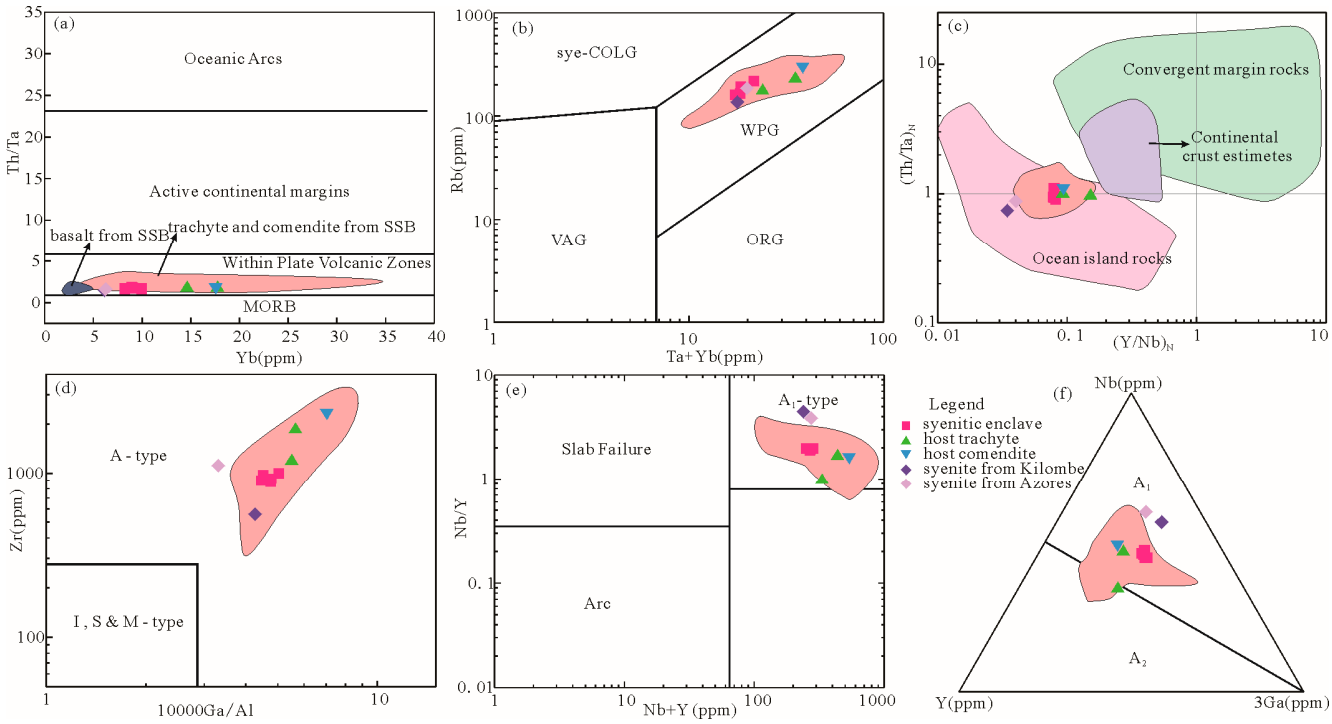

Figure 7. Trace element distribution diagrams for syenitic enclaves from the Sanshui Basin. (**a**) Th/Ta vs. Yb diagram after [61]. (**b**) Rb vs. Ta + Yb diagram after [62], where WPG = within plate granite, VAG = volcanic arc granite, ORG = ocean ridge granite, and syn-COLG = syn-collision granite. (**c**) $(Th/Ta)_N$ vs. $(Y/Nb)_N$ diagram after [63]. (**d**) Zr vs. 10,000 Ga/Al diagram after [60]. (**e**) Nb/Y vs. Nb + Y diagram after [64]. (**f**) Nb-Y-Ce diagram after [60]. A_1 field represents mantle-derived granites, A_2 field represents crustal-derived granites.

5.2. Petrogenesis of the Syenitic Enclaves

The syenitic enclaves had a high Nb/U ratio (Table 2) and Nb-Ta enrichment, which was similar to the characteristics of the basaltic rocks in the Sanshui Basin [39,43]; this indicated that the syenitic enclaves had a genetic relationship with the basaltic rocks. The Pb anomaly was not obvious, which indicated insignificant contamination by the crustal materials [66]. The Ba, Sr, P, Eu, and Ti depletion reflected the fractional crystallization of plagioclase, alkaline feldspar, apatite, and Fe-Ti oxides during the magmatic evolution. In addition, the low concentrations of transition metal elements (Ni, Co, Cr, Sc) also indicated the crystallization of mafic minerals (olivine, clinopyroxene). Therefore, mass-balance and

thermodynamic modeling were applied to investigate whether the syenitic composition could be created from the basaltic parental magma via fractional crystallization.

The basalt sample 14ss012-1 [67], which had a higher MgO content (7.35 wt%), was selected as the parental composition for the mass-balance calculation. The mass-balance calculation results showed that the sum of the squared residuals was 0.85 (Table 6), which indicated that syenite can be produced via fractional crystallization. The calculated results indicated that the evolution from 14ss012-1 to 19ss036-1 could be calculated via 74% fractional crystallization of a phase assemblage including olivine (11%), clinopyroxene (14%), plagioclase (39%), apatite (2%), magnetite (5%), and ilmenite (3%). The calculated trace element concentrations were broadly compatible with the results of 74% fractional crystallization of the syenitic enclaves, the diversity in the various trace elements may have been caused by the presence of accessory minerals or alterations (Table 6 and Figure 8).

Table 6. Mass-balance modeling input parameters and results.

Model	14ss012-1	19ss036-1	Cpx	Ol	Pl	Ap	Ilm	Mag	Odiff	Cdiff	RES
SiO_2	47.41	64.12	48.56	38.25	51.39	0.21	0.28	0.27	16.72	16.50	0.22
TiO_2	2.79	0.49	1.4	0	0.13	0.09	51.89	26.65	−2.30	−2.42	0.12
Al_2O_3	17.07	17.11	6.87	0.03	30.32	0.02	0.11	0.94	0.04	0.00	0.03
FeOt	10.00	5.11	7.22	22.86	0.61	0.8	45.25	70.58	−4.89	−5.01	0.11
MnO	0.15	0.06	0.13	0.35	0.01	0.1	0.74	1.45	−0.09	−0.11	0.02
MgO	7.31	0.14	14.78	38.15	0.08	0.36	1.51	0.05	−7.17	−7.18	0.01
CaO	8.76	0.86	20.44	0.24	12.75	52.24	0.14	0.03	−7.90	−7.87	−0.03
Na_2O	3.50	7.09	0.58	0.06	4.04	0.09	0.03	0.03	3.59	3.62	−0.03
K_2O	2.26	4.96	0.02	0.05	0.65	0.03	0.06	0	2.70	3.43	−0.73
P_2O_5	0.74	0.05	0	0	0.03	46.07	0	0	−0.69	−0.97	0.28
Total	100.00	100.00	100	100	100	100	100	100			
SSR											0.59
Wt%			11.44	14.46	39.30	2.14	2.57	4.53			74.45
Nb	89.7	188							188	302	114
ZrS	150	972							972	539	−433
Sr	874	22.8							22.8	3	−19.8
Rb	45.8	165							165	164	−1
Y	26.1	96							96	96	0
Ni	90	0.5							0.5	0	−0.5
Th	3.8	19.4							19.4	14	−5.4

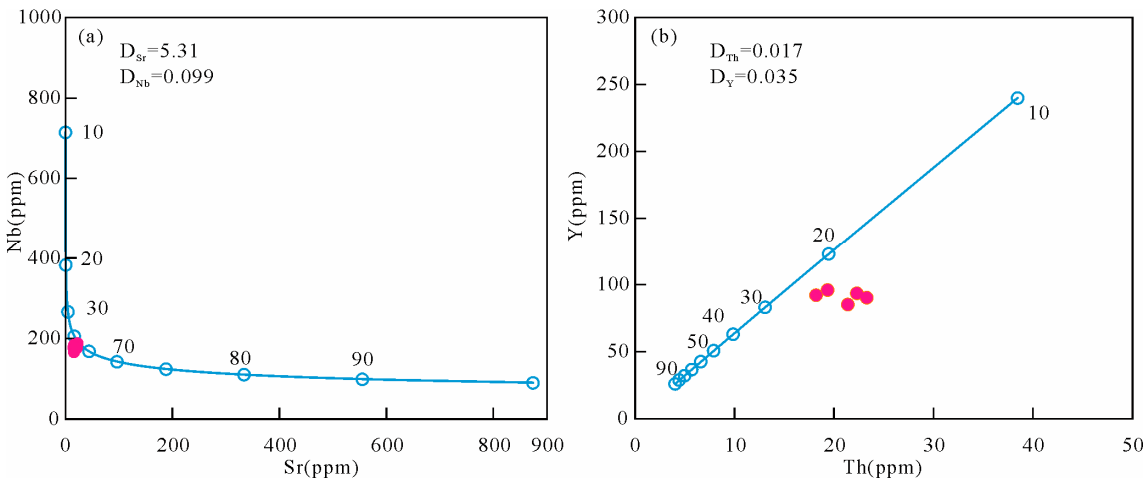

Figure 8. Trace elements variation diagrams with fractional crystallization model for the syenetic enclaves from the Sanshui Basin. (**a**) Nb vs. Sr, (**b**) Y vs. Th. Circled intervals represent 10% fractionation. Partition coefficients were calculated from Table 6.

The parental composition of 14ss012-1 and mineral geochemical composition are from [67], Ol = olivine, Cpx = clinopyroxene, Pl = plagioclase, Ap = apatite, Ilm = ilmenite, Mag = magnetite. Odiff = observed different, Cdiff = calculated different, SSR = the sum of the squared residuals, and Wt% = the weight % of removed phase. Trace element calculation based on the Rayleigh fractionation model, and the mineral partition coefficients were cited from the GERM Database (https://kdd.earthref.org/KdD/ accessed on 20 April 2023) and showed in Table S1.

The thermodynamic magma chamber simulator (MCS) [68] was applied to model the fractional crystallization from the basaltic to syenitic magma. Basalt (17ss060-1, [69]) was selected as the starting composition. The basalt was not primitive [70] due the low Ni (less than 130 ppm), Cr (less than 247 ppm), and Mg# (42–61) [67] content, which indicated that basaltic magma underwent fractional crystallization of olivine and clinopyroxene. The oxygen fugacity of the starting composition was set under the fayalite–magnetite–quartz (FMQ) buffer, the oxygen fugacity of cogenetic trachyte calculated by Chen [41], and the pressure and initial water content were 1 kbar and 0.5–2 wt%, respectively. The liquidus temperature was 1130 °C when the olivine crystallized, followed by plagioclase, clinopyroxene, magnetite, apatite, and ilmenite. The approximate composition range of the syenitic enclave was 880 °C to 930 °C (Figure 9), which corresponded to 64–69 wt% of the total crystalline phase, including olivine (~5 wt%), clinopyroxene (~20 wt%), plagioclase (34–38 wt%), apatite (~0.5 wt%), magnetite (~11 wt%), and ilmenite (~0.5 wt%), which was similar to the major elements mass-balance result, which again indicated the genesis of the fractional crystallization of the syenitic enclaves.

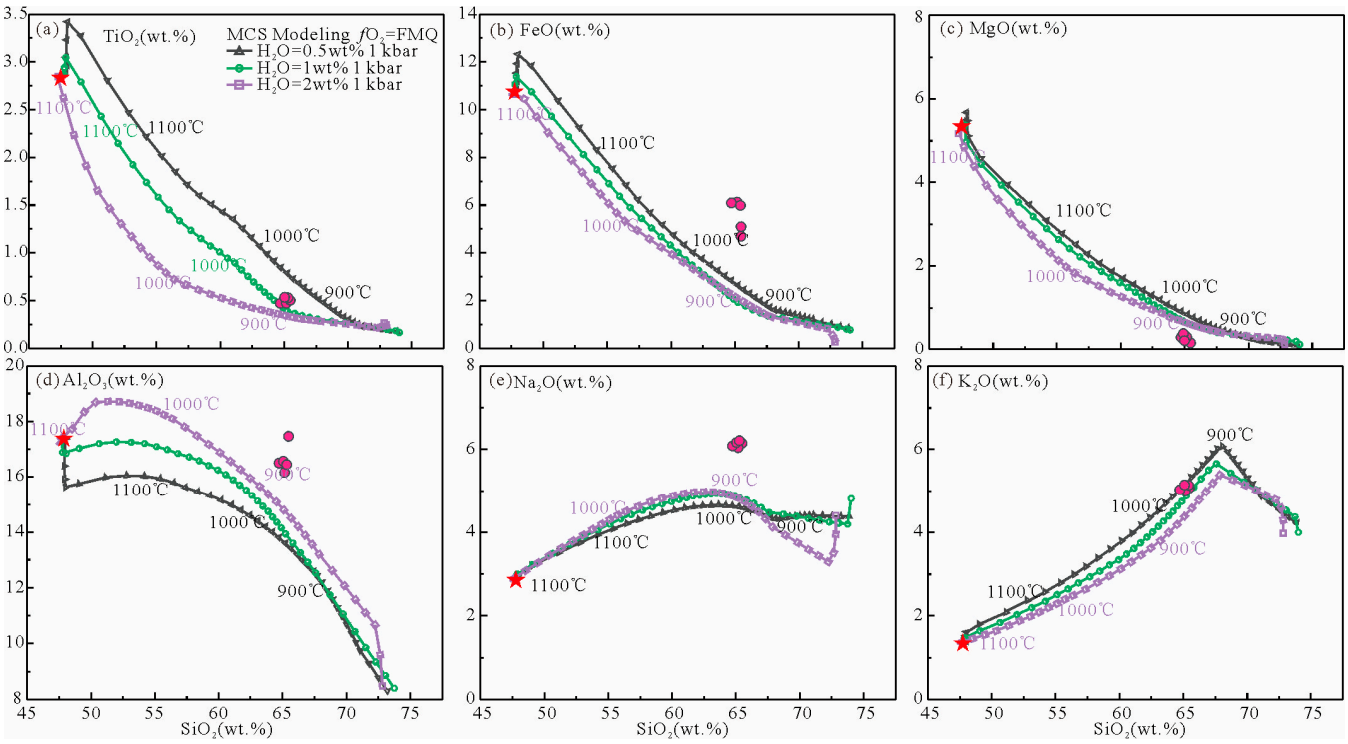

Figure 9. MCS fractional crystallization modeling of basaltic parental composition (17ss060-1) from the Sanshui Basin showing the major oxide element evolution curves under the set condition. The models show the liquid compositions at 10°C intervals at 0.5 wt% H_2O (grey triangle), 1 wt% H_2O (green circle), and 2 wt% H_2O (purple square).

5.3. Origin of the Syenitic Enclaves

The geochemical characteristics of the syenitic enclaves host rocks in the Sanshui Basin suggested that they were produced via prolonging fractional crystallization from the basaltic magma in the shallow crust [39,44]. Many similarities in the geochemical

characteristics of the syenitic enclaves and their host rocks existed, this combined with their similar mineral assemblages and mineralogical characteristics demonstrated that the syenitic enclaves were crystallized from the same magma chamber with the peralkaline felsic volcanic rocks, and thus were "cogenetic". Three models of the magmatic enclaves crystallized from the cogenetic magma are advocated: (1) the cumulated crystals of early minerals [11,13], (2) the injection of cogenetic magma [32], and (3) the fragment of marginal crystalline phases [29,30,37]. The distinctive boundaries, alkali feldspar grain size plunges, fibrous alkaline feldspar, and acicular amphibole were observed at the boundary of the host trachyte/comendite and syenitic enclaves. We think that the syenitic enclaves likely originated from the crystallization of the cogenetic trachytic magma, and the main evidence for this is as follows:

Petrographically, no cumulated and compacted crystal textures of tabular alkali feldspar were observed in the thin sections (Figure 3). Additionally, no glass component was observed in the alkali feldspar framework, but rather anhedral sodium hornblende and aegirine, which indicated that the syenite formed via crystallization or nearly crystallization. Syenitic enclaves are mainly found in trachyte, followed by comendite. Due to the similar crystallization temperature and pressure conditions of syenite and trachyte were estimated [57], if the two types of magmas mix, rocks with different crystallinity are unlikely to form. Thus, the undercooling texture of syenitic enclaves hosted in trachyte (Figure 3c,d) may indicate an earlier interaction with the cold wall-rock rather a trachytic magma injection. Therefore, the syenite enclaves hosted in the trachyte were more likely originated from earlier crystallization prior to the trachytic magma [29,37], the granular and porphyritic structures were probably represented the various temperatures within the magma chamber, and the alkali feldspar in the syenite coursing in a relatively stable temperature and pressure condition compared with the syenite porphyry. If the syenitic magma mixed with the comenditic magma, the hotter syenitic magma injected into the colder comenditic magma, a high degree of undercooling would have led to the undercooling textures in the syenitic enclaves, and this would have led to the buildup of volatiles and second boiling in the comenditic melt [32,71]. As a result, many vesicles and undercooling textures would have been formed in syenitic enclaves as in Pantelleria [32]. However, the magmatic enclaves hosted in both trachyte and comendite in the Sanshui Basin had few vesicles, and the enclaves with an undercooling texture only were observed in the enclaves hosted in trachyte (19ss036, Figure 3c,d). Therefore, we think that the syenitic enclaves may resulted from the in situ crystallization of earlier trachytic magma batches.

Geochemically, the major element and trace element characteristics of the syenitic enclaves were similar to those of the host trachyte; namely, they had a similar SiO_2 content as well as trace element and rare earth element normalized patterns. More than 85% alkaline feldspar was in syenitic enclaves, and the negative Eu anomaly would have been insignificant or even positive if these syenitic enclaves had cumulated genesis, the accumulation of alkaline feldspaer would have buffered the negative Eu anomaly [29] owing the higher Eu partition coefficient ($Kd_{Eu}{}^{afs/liq} = 0.37$), compared with Sm ($Kd_{Sm}{}^{afs/liq} = 0.03$) and Gd ($Kd_{Gd}{}^{afs/liq} = 0.03$) [72].However, Eu anomalies of the syenitic enclaves were not significantly correlated with their host rock; the syenitic enclaves exhibited equal and lower Eu anomalies than those of the trachytes in the Sanshui Basin. Therefore, the syenitic enclaves were unlikely to be the cumulated crystal genesis.

Earlier researchers have suggested that syenitic enclaves in alkaline volcanic systems are caused by in situ crystallization [29,30,34,37]. Some researchers describe these cogenetic enclaves as "autoliths" (auto = self, lith = stone) [13,29], whereby the name represents the fact that they have the same origin as the host rock.

5.4. Implications for the Alkaline Volcanic System

The bimodal volcanic rocks in the Sanshui Basin provide a unique opportunity to study the magma plumbing system of alkaline volcanic systems in continental rifts, and studying syenitic enclaves is essential to refine the magma plumbing system.

The clinopyroxene in the basalt suggested the presence of a basaltic magma reservoir that continues from the lower crust to the shallow crust [57]. Both the geochemical and thermometer results indicated that the felsic volcanic rocks and syenitic enclaves were products of the basaltic magma that underwent protracted fractional crystallization in the magma reservoir of the upper crust depths. They had similar mineral assemblages: both were dominated by alkali feldspar, followed by sodium amphibole and clinopyroxene, and minor Ti-Fe oxides. In the deep magma reservoir, the basaltic magma continuously underwent fractional crystallization and evolved to trachytic magma; when a batch of trachytic magma is produced, this trachytic magma is first in situ crystallized on the roof and walls of the magma reservoir as a crust [37], and it simultaneously forms a barrier against the exchange of energy and material between trachytic magma and wall-rocks (Figure 10). The underplated basaltic magma maintained near crystallization and provided materials for the upper magma reservoirs, which allowed the trachytic melt to remain in the shallow crustal reservoir longer and thereby eventually forming the bimodal volcanic rocks [29,37]. Thus, the cogenetic syenitic enclaves and trachyte were formed under different crystallization conditions within the magma reservoir, syenitic enclaves were formed via in situ crystallization on the roof and walls of the magma reservoir where heat and energy were most easily lost, and trachyte and comendite resulted from surface eruptions, which is similar to how the enclaves in the volcanic rocks of the Pantelleria, Azores, and East African rift valleys are formed [30,32,34,35,37] The high Mg# clinopyroxene in host trachyte and the embayed alkali feldspar phenocryst in trachyte and comendite suggest magma recharge [57] and mixing, whereby the injection of basaltic magma triggered local heating and eventually induced a trachytic and comenditic magma eruption, and the ascending trachytic and comenditic magma disaggregated the in situ syenitic crystallized crust, which was brought to the surface as syenitic enclaves.

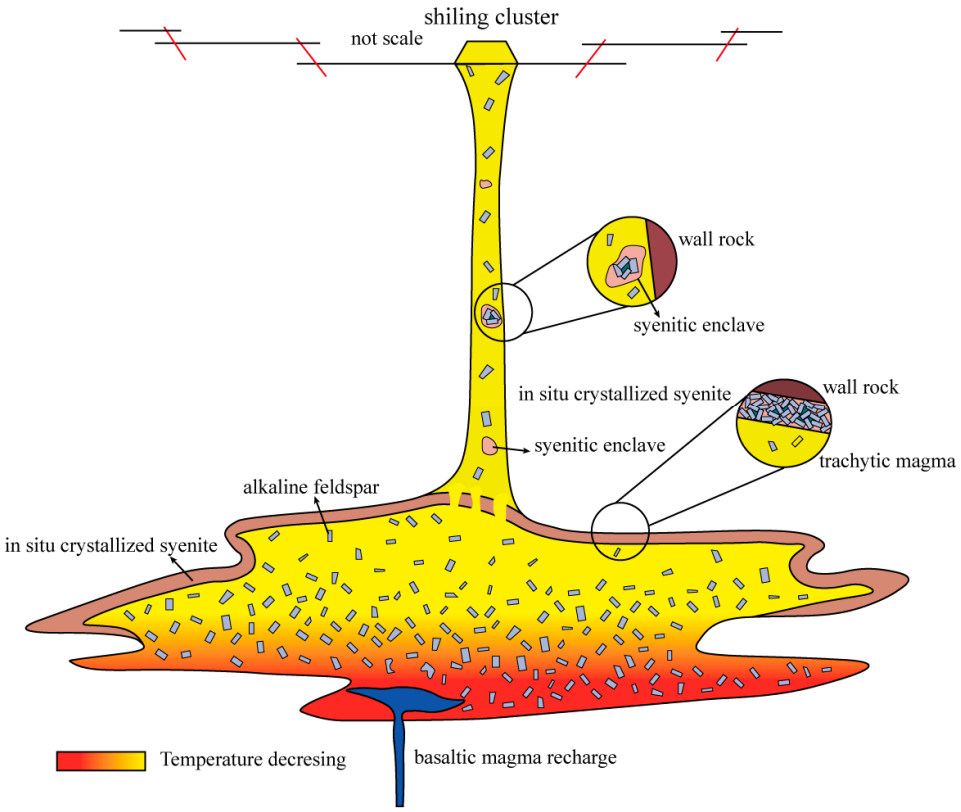

Figure 10. Schematic model of the magma plumbing system associated with bimodal volcanic rocks in the Sanshui Basin.

6. Conclusions

1. The peralkaline felsic volcanic rocks in the Sanshui Basin commonly contain syenite and syenite porphyry enclaves. The petrological, geochemical, and mineralogical characteristics of the syenite and syenite porphyry enclaves indicated that they were cogenetic with the host trachyte and comendite and were formed by the fractional crystallization of the basaltic magma.
2. The syenitic enclaves are the results of in situ crystallization of the trachytic magma in the shallow crust according to the thermobarometric calculation and petrological texture. The recharge of the basaltic magma triggered a trachytic and comenditic eruption, and the ascending trachytic and comenditic magma disaggregated the in situ syenitic crystallized crust which was brought to the surface as syenitic enclaves.

Supplementary Materials: The following supporting information can be downloaded at: https://www.mdpi.com/article/10.3390/min13050590/s1, Table S1: Partition coefficients used for trace element modeling [73–80].

Author Contributions: Conceptualization, P.C. and N.F.; methodology, P.C. and Z.Z.; investigation, P.C. and Z.Z.; resources, N.F.; writing—original draft preparation, P.C.; writing—review and editing, N.F. and B.Q.; visualization, B.Q.; supervision, B.Q.; project administration, N.F.; funding acquisition, N.F. All authors have read and agreed to the published version of the manuscript.

Funding: This research was funded by National Natural Science Foundation of China (No. 41572207) and Fundamental Research Funds for National Universities, Xichang University (No. YBZ202264).

Data Availability Statement: The original contributions presented in the study are included in the article.

Acknowledgments: We are grateful to Yu Zhang, and Yang Liu for their help in the field works. We thank Hui Zhang and Jianbing Duan for help in EPMA analyze at ECUT.

Conflicts of Interest: The authors declare no conflict of interest.

References

1. Perugini, D.; Poli, G. The Mixing of Magmas in Plutonic and Volcanic Environments: Analogies and Differences. *Lithos* **2012**, *153*, 261–277. [CrossRef]
2. Didier, J. *Granites and Their Enclaves: The Bearing of Enclaves on the Origin of Granites: Developments in Petrology 3*; Elsevier: Amsterdam, The Netherlands, 1973.
3. Yang, J.H.; Wu, F.Y.; Wilde, S.A.; Xie, L.W.; Yang, Y.H.; Liu, X.M. Tracing Magma Mixing in Granite Genesis: In Situ U–Pb Dating and Hf-Isotope Analysis of Zircons. *Contrib. Mineral. Petrol.* **2007**, *153*, 177–190. [CrossRef]
4. Cheng, Y.B.; Spandler, C.; Mao, J.W.; Rusk, B.G. Granite, Gabbro and Mafic Microgranular Enclaves in the Gejiu Area, Yunnan Province, China: A Case of Two-Stage Mixing of Crust- and Mantle-Derived Magmas. *Contrib. Mineral. Petrol.* **2012**, *164*, 659–676. [CrossRef]
5. Flood, R.H.; Shaw, S.E. Microgranitoid Enclaves in the Felsic Looanga Monzogranite, New England Batholith, Australia: Pressure Quench Cumulates. *Lithos* **2014**, *198–199*, 92–102. [CrossRef]
6. Dan, W.; Wang, Q.; Wang, X.C.; Liu, Y.; Wyman, D.A.; Liu, Y.S. Overlapping Sr–Nd–Hf–O Isotopic Compositions in Permian Mafic Enclaves and Host Granitoids in Alxa Block, NW China: Evidence for Crust–Mantle Interaction and Implications for the Generation of Silicic Igneous Provinces. *Lithos* **2015**, *230*, 133–145. [CrossRef]
7. Qin, J.-F.; Lai, S.-C.; Diwu, C.-R.; Ju, Y.-J.; Li, Y.-F. Magma Mixing Origin for the Post-Collisional Adakitic Monzogranite of the Triassic Yangba Pluton, Northwestern Margin of the South China Block: Geochemistry, Sr–Nd Isotopic, Zircon U–Pb Dating and Hf Isotopic Evidences. *Contrib. Mineral. Petrol.* **2010**, *159*, 389–409. [CrossRef]
8. Chappell, B.W.; White, A.J.R.; Wyborn, D. The Importance of Residual Source Material (Restite) in Granite Petrogenesis. *J. Petrol.* **1987**, *28*, 1111–1138. [CrossRef]
9. Chappell, B.W.; Wyborn, D. Origin of Enclaves in S-Type Granites of the Lachlan Fold Belt. *Lithos* **2012**, *154*, 235–247. [CrossRef]
10. Wyborn, D. Reply—Origin of Enclaves in S-Type Granites of the Lachlan Fold Belt. *Lithos* **2013**, *175–176*, 353–354. [CrossRef]
11. Lee, C.-T.A.; Morton, D.M.; Farner, M.J.; Moitra, P. Field and Model Constraints on Silicic Melt Segregation by Compaction/Hindered Settling: The Role of Water and Its Effect on Latent Heat Release. *Am. Mineral.* **2015**, *100*, 1762–1777. [CrossRef]
12. Niu, Y.L.; Zhao, Z.D.; Zhu, D.C.; Mo, X.X. Continental Collision Zones Are Primary Sites for Net Continental Crust Growth—A Testable Hypothesis. *Earth-Sci. Rev.* **2013**, *127*, 96–110. [CrossRef]

13. Shellnutt, J.G.; Jahn, B.-M.; Dostal, J. Elemental and Sr–Nd Isotope Geochemistry of Microgranular Enclaves from Peralkaline A-Type Granitic Plutons of the Emeishan Large Igneous Province, SW China. *Lithos* **2010**, *119*, 34–46. [CrossRef]
14. Donaire, T.; Pascual, E.; Pin, C.; Duthou, J.-L. Microgranular Enclaves as Evidence of Rapid Cooling in Granitoid Rocks: The Case of the Los Pedroches Granodiorite, Iberian Massif, Spain. *Contrib. Mineral. Petrol.* **2005**, *149*, 247–265. [CrossRef]
15. Maas, R.; Nicholls, I.A.; Legg, C. Igneous and Metamorphic Enclaves in the S-Type Deddick Granodiorite, Lachlan Fold Belt, SE Australia: Petrographic, Geochemical and Nd-Sr Isotopic Evidence for Crustal Melting and Magma Mixing. *J. Petrol.* **1997**, *38*, 815–841. [CrossRef]
16. Zhang, S.H.; Zhao, Y. Cogenetic Origin of Mafic Microgranular Enclaves in Calc-Alkaline Granitoids: The Permian Plutons in the Northern North China Block. *Geosphere* **2017**, *13*, 482–517. [CrossRef]
17. Bullock, L.A.; Gertisser, R.; O'Driscoll, B.; Harland, S. Magmatic Evolution and Textural Development of the 1739 CE Pietre Cotte Lava Flow, Vulcano, Italy. *J. Volcanol. Geotherm. Res.* **2019**, *372*, 1–23. [CrossRef]
18. Elburg, M.A. Genetic Significance of Multiple Enclave Types in a Peraluminous Ignimbrite Suite, Lachlan Fold Belt, Australia. *J. Petrol.* **1996**, *37*, 1385–1408. [CrossRef]
19. Hadimi, I.; Youbi, N.; Ait Lahna, A.; Bensalah, M.K.; Moutbir, O.; Mata, J.; Doblas, M.; Tassinari, C.C.G.; Gaggero, L.; Basei, M.A.S.; et al. U–Pb Zircon Geochronological and Petrologic Constraints on the Post-Collisional Variscan Volcanism of the Tiddas-Souk Es-Sebt Des Aït Ikko Basin (Western Meseta, Morocco). *Minerals* **2021**, *11*, 1099. [CrossRef]
20. Hamada, M.; Hanyu, T.; McIntosh, I.M.; Tejada, M.L.G.; Chang, Q.; Kaneko, K.; Kimura, J.-I.; Kiyosugi, K.; Miyazaki, T.; Nakaoka, R.; et al. Evolution of Magma Supply System beneath a Submarine Lava Dome after the 7.3-Ka Caldera-Forming Kikai-Akahoya Eruption. *J. Volcanol. Geotherm. Res.* **2023**, *434*, 107738. [CrossRef]
21. Jofré, C.B.; Caffe, P.J.; Trumbull, R.B.; Maro, G.; Schmitt, A.K.; Sarchi, C.; Flores, P.I.; Peralta Arnold, Y.J.; Franco, M.G.; Lucassen, F. Petrogenesis of Peraluminous Magmas in the Central Andean Backarc: The Huayra Huasi Volcanic Complex, NW Argentina. *Int. J. Earth Sci.* **2021**, *110*, 2725–2754. [CrossRef]
22. Kovacs, M.; Fülöp, A.; Seghedi, I.; Pécskay, Z. Architecture of Volcanic Plumbing Systems Inferred from Thermobarometry: A Case Study from the Miocene Gutâi Volcanic Zone in the Eastern Carpathians, Romania. *Lithos* **2021**, *396–397*, 106191. [CrossRef]
23. Sharpe, M.S.; Barker, S.J.; Rooyakkers, S.M.; Wilson, C.J.N.; Chambefort, I.; Rowe, M.C.; Schipper, C.I.; Charlier, B.L.A. A Sulfur and Halogen Budget for the Large Magmatic System beneath Taupō Volcano. *Contrib. Mineral. Petrol.* **2022**, *177*, 95. [CrossRef]
24. Shaw, C.S.J. Dissolution—Reprecipitation Reactions as a Mechanism for Magma Contamination: An Example from Interaction of Partially Melted Sanidine Megacrysts and Clinopyroxene Phenocrysts in Nephelinite from Graulei, West Eifel Volcanic Field, Germany. *Lithos* **2021**, *404–405*, 106486. [CrossRef]
25. Taussi, M.; Godoy, B.; Piscaglia, F.; Morata, D.; Agostini, S.; Le Roux, P.; González-Maurel, O.; Gallmeyer, G.; Menzies, A.; Renzulli, A. The Upper Crustal Magma Plumbing System of the Pleistocene Apacheta-Aguilucho Volcanic Complex Area (Altiplano-Puna, Northern Chile) as Inferred from the Erupted Lavas and Their Enclaves. *J. Volcanol. Geotherm. Res.* **2019**, *373*, 179–198. [CrossRef]
26. Yoshida, K.; Tamura, Y.; Sato, T.; Hanyu, T.; Usui, Y.; Chang, Q.; Ono, S. Variety of the Drift Pumice Clasts from the 2021 Fukutoku-Oka-No-Ba Eruption, Japan. *Isl. Arc* **2022**, *31*, e12441. [CrossRef]
27. Fedele, L.; Tarzia, M.; Belkin, H.E.; Vivo, B.D.; Lima, A.; Lowenstern, J.B. Chapter 7 Magmatic-Hydrothermal Fluid Interaction and Mineralization in Alkali-Syenite Nodules from the Breccia Museo Pyroclastic Deposit, Naples, Italy. In *Developments in Volcanology*; Elsevier: Amsterdam, The Netherlands, 2006; Volume 9, pp. 125–161. ISBN 978-0-444-52175-0.
28. Giannetti, B.; Luhr, J.F. The White Trachytic Tuff of Roccamonfina Volcano (Roman Region, Italy). *Contrib. Mineral. Petrol.* **1983**, *84*, 235–252. [CrossRef]
29. Jeffery, A.J.; Gertisser, R.; Self, S.; Pimentel, A.; O'Driscoll, B.; Pacheco, J.M. Petrogenesis of the Peralkaline Ignimbrites of Terceira, Azores. *J. Petrol.* **2017**, *58*, 2365–2401. [CrossRef]
30. Jeffery, A.J.; Gertisser, R.; O'Driscoll, B.; Pacheco, J.M.; Whitley, S.; Pimentel, A.; Self, S. Temporal Evolution of a Post-Caldera, Mildly Peralkaline Magmatic System: Furnas Volcano, Sao Miguel, Azores. *Contrib. Mineral. Petrol.* **2016**, *171*, 42. [CrossRef]
31. Jones, W.B. Syenite Boulders Associated with Kenyan Trachyte Volcanoes. *Lithos* **1979**, *12*, 89–97. [CrossRef]
32. Landi, P.; Rotolo, S.G. Cooling and Crystallization Recorded in Trachytic Enclaves Hosted in Pantelleritic Magmas (Pantelleria, Italy): Implications for Pantellerite Petrogenesis. *J. Volcanol. Geotherm. Res.* **2015**, *301*, 169–179. [CrossRef]
33. Park, J.; Lim, H.; Myeong, B.; Jang, Y.D. Syenite from Ulleung Island: As a Window for Pre-Eruptive Shallow Alkaline Magma Dynamics. *Lithos* **2020**, *356–357*, 105342. [CrossRef]
34. Ridolfi, F.; Renzulli, A.; Macdonald, R.; Upton, B.G.J. Peralkaline Syenite Autoliths from Kilombe Volcano, Kenya Rift Valley: Evidence for Subvolcanic Interaction with Carbonatitic Fluids. *Lithos* **2006**, *91*, 373–392. [CrossRef]
35. Ridolfi, F.; Renzulli, A.; Santi, P.; Upton, B.G.J. Evolutionary Stages of Crystallization of Weakly Peralkaline Syenites: Evidence from Ejecta in the Plinian Deposits of Agua de Pau Volcano (São Miguel, Azores Islands). *Mineral. Mag.* **2003**, *67*, 749–767. [CrossRef]
36. Turbeville, B.N. Sidewall Differentiation in an Alkalic Magma Chamber: Evidence from Syenite Xenoliths in Tuffs of the Latera Caldera, Italy. *Geol. Mag.* **1993**, *130*, 453–470. [CrossRef]
37. Widom, E.; Gill, J.B.; Schmincke, H.-U. Syenite Nodules as a Long-Term Record of Magmatic Activity in Agua de Pao Volcano, Sao Miguel, Azores. *J. Petrol.* **1993**, *34*, 929–953. [CrossRef]
38. Macdonald, R.; White, J.C.; Belkin, H.E. Peralkaline Silicic Extrusive Rocks: Magma Genesis, Evolution, Plumbing Systems and Eruption. *C. R. Geosci.* **2021**, *353*, 7–59. [CrossRef]

39. Zhou, H.M.; Xiao, L.; Dong, Y.X.; Wang, C.Z.; Wang, F.Z.; Ni, P.Z. Geochemical and Geochronological Study of the Sanshui Basin Bimodal Volcanic Rock Suite, China: Implications for Basin Dynamics in Southeastern China. *J. Asian Earth Sci.* **2009**, *34*, 178–189. [CrossRef]
40. Bureau of Geology and Mineralogy of Guangdong Province. *Regional Geology of the Guangdong Province*; Geology Publishing House: Beijing, China, 1988.
41. Chen, P.J. Petrogenesis of the Eocene Peralkaline Felsic Volcanic Rocks in Sanshui Basin, Guangdong and Relationship with the Opening of the South China Sea. Ph.D. Thesis, China University of Geosciences (Beijing), Beijing, China, 2022.
42. Li, J.H.; Zhang, Y.Q.; Dong, S.W.; Johnston, S.T. Cretaceous Tectonic Evolution of South China: A Preliminary Synthesis. *Earth-Sci. Rev.* **2014**, *134*, 98–136. [CrossRef]
43. Chung, S.L.; Cheng, H.; Jahn, B.M.; O'Reilly, S.Y.; Zhu, B.Q. Major and Trace Element, and Sr-Nd Isotope Constraints on the Origin of Paleogene Volcanism in South China Prior to the South China Sea Opening. *Lithos* **1997**, *40*, 203–220. [CrossRef]
44. Xiao, L.; Zhou, H.M.; Dong, Y.X.; Zeng, G.C.; Wang, F.Z. Geochemistry and Petrogenesis of Cenozoic Olcanic Rocks from Sanshui Basin: Implications for Spatial and Temporal Ariation of Rock Types and Constraints on the Formation of South China Sea. *Geotecton. Et Metallog.* **2006**, *30*, 72–81.
45. White, J.C.; Holt, G.S.; Parker, D.F.; Ren, M. Trace-Element Partitioning between Alkali Feldspar and Peralkalic Quartz Trachyte to Rhyolite Magma. Part I: Systematics of Trace-Element Partitioning. *Am. Mineral.* **2003**, *88*, 316–329. [CrossRef]
46. Streckeisen, A. To Each Plutonic Rock Its Proper Name. *Earth-Sci. Rev.* **1976**, *12*, 1–33. [CrossRef]
47. De la Roche, H.; Leterrier, J.; Grandclaude, P.; Marchal, M. A Classification of Volcanic and Plutonic Rocks Using R1R2 -Diagram and Major-Element Analyses—Its Relationships with Current Nomenclature. *Chem. Geol.* **1980**, *29*, 183–210. [CrossRef]
48. Frost, C.D.; Frost, B.R. On Ferroan (A-Type) Granitoids: Their Compositional Variability and Modes of Origin. *J. Petrol.* **2011**, *52*, 39–53. [CrossRef]
49. Macdonald, R.; Belkin, H.E.; Fitton, J.G.; Rogers, N.W.; Nejbert, K.; Tindle, A.G.; Marshall, A.S. The Roles of Fractional Crystallization, Magma Mixing, Crystal Mush Remobilization and Volatile–Melt Interactions in the Genesis of a Young Basalt–Peralkaline Rhyolite Suite, the Greater Olkaria Volcanic Complex, Kenya Rift Valley. *J. Petrol.* **2008**, *49*, 1515–1547. [CrossRef]
50. McDonough, W.F.; Sun, S.S. The Composition of the Earth. *Chem. Geol.* **1995**, *120*, 223–253. [CrossRef]
51. Fuhrman, M.L.; Lindsley, D.H. Ternary-Feldspar Modeling and Thermometry. *Am. Mineral.* **1988**, *73*, 201–215.
52. Morimoto, N.; Fabries, J.; Ferguson, A.K.; Ginzburg, I.V.; Ross, M.; Seifert, F.A.; Zussman, J.; Aoki, K.; Gottardi, G. Nomenclature of Pyroxenes. *Am. Mineral.* **1988**, *73*, 1123–1133.
53. Hawthorne, F.C.; Oberti, R.; Harlow, G.E.; Maresch, W.V.; Martin, R.F.; Schumacher, J.C.; Welch, M.D. Nomenclature of the Amphibole Supergroup. *Am. Mineral.* **2012**, *97*, 2031–2048. [CrossRef]
54. Putirka, K.D. Thermometers and Barometers for Volcanic Systems. *Rev. Mineral. Geochem.* **2008**, *69*, 61–120. [CrossRef]
55. Masotta, M.; Mollo, S.; Freda, C.; Gaeta, M.; Moore, G. Clinopyroxene–Liquid Thermometers and Barometers Specific to Alkaline Differentiated Magmas. *Contrib. Mineral. Petrol.* **2013**, *166*, 1545–1561. [CrossRef]
56. Jorgenson, C.; Higgins, O.; Petrelli, M.; Bégué, F.; Caricchi, L. A Machine Learning-Based Approach to Clinopyroxene Thermobarometry: Model Optimization and Distribution for Use in Earth Sciences. *JGR Solid Earth* **2022**, *127*, e2021JB022904. [CrossRef] [PubMed]
57. Chen, P.J.; Fang, N.Q.; Yuan, X.B. Geochemical Insights from Clinopyroxene Phenocrysts into the Magma Evolution of an Alkaline Magmatic System from the Sanshui Basin, South China. *Minerals* **2021**, *11*, 1295. [CrossRef]
58. Li, X.Y.; Zhang, C.; Behrens, H.; Holtz, F. Calculating Amphibole Formula from Electron Microprobe Analysis Data Using a Machine Learning Method Based on Principal Components Regression. *Lithos* **2020**, *362–363*, 105469. [CrossRef]
59. Papoutsa, A.; Pe-Piper, G. Geochemical Variation of Amphiboles in A-Type Granites as an Indicator of Complex Magmatic Systems: Wentworth Pluton, Nova Scotia, Canada. *Chem. Geol.* **2014**, *384*, 120–134. [CrossRef]
60. Eby, G.N. Chemical Subdivision of the A-Type Granitoids:Petrogenetic and Tectonic Implications. *Geology* **1992**, *20*, 641–644. [CrossRef]
61. Schandl, E.S.; Gorton, M.P. Application of High Field Strength Elements to Discriminate Tectonic Settings in VMS Environments. *Econ. Geol.* **2002**, *97*, 629–642. [CrossRef]
62. Whalen, J.B.; Currie, K.L.; Chappell, B.W. A-Type Granites: Geochemical Characteristics, Discrimination and Petrogenesis. *Contrib. Mineral. Petrol.* **1987**, *95*, 407–419. [CrossRef]
63. Moreno, J.A.; Molina, J.F.; Montero, P.; Abu Anbar, M.; Scarrow, J.H.; Cambeses, A.; Bea, F. Unraveling Sources of A-Type Magmas in Juvenile Continental Crust: Constraints from Compositionally Diverse Ediacaran Post-Collisional Granitoids in the Katerina Ring Complex, Southern Sinai, Egypt. *Lithos* **2014**, *192–195*, 56–85. [CrossRef]
64. Whalen, J.B.; Hildebrand, R.S. Trace Element Discrimination of Arc, Slab Failure, and A-Type Granitic Rocks. *Lithos* **2019**, *348–349*, 105179. [CrossRef]
65. Basua, A.A.E.; Ma, C.; Nguo, K.S.; Wang, L.-X.; Lentz, D.R.; Mukherjee, S.; Nformidah-Ndah, S.S.; Yomeun, B.S. Petrogenesis and Tectonic Setting of A-Type Granites in the Babouri-Figuil Magmatic Complex (North Cameroon): Constraints from Whole Rock Geochemistry, Zircon UPb Geochronology and Sr-Nd-Hf Isotopes. *Lithos* **2022**, *414–415*, 106618. [CrossRef]
66. Yu, Y.Y.; Zong, K.Q.; Yuan, Y.; Klemd, R.; Wang, X.-S.; Guo, J.L.; Xu, R.; Hu, Z.C.; Liu, Y.S. Crustal Contamination of the Mantle-Derived Liuyuan Basalts: Implications for the Permian Evolution of the Southern Central Asian Orogenic Belt. *J. Earth Sci.* **2022**, *33*, 1081–1094. [CrossRef]

67. Yuan, X.B. The Record of Cenozoic Magmatism in Sanshui Basin and Its Relationship with the Early Tectonic Evolution Stage of the South China Sea. Ph.D. Thesis, China University of Geosciences (Beijing), Beijing, China, 2019.
68. Bohrson, W.A.; Spera, F.J.; Heinonen, J.S.; Brown, G.A.; Scruggs, M.A.; Adams, J.V.; Takach, M.K.; Zeff, G.; Suikkanen, E. Diagnosing Open-System Magmatic Processes Using the Magma Chamber Simulator (MCS): Part I—Major Elements and Phase Equilibria. *Contrib. Mineral. Petrol.* **2020**, *175*, 104. [CrossRef]
69. Zhang, Y.; Fang, N.Q. Source Characteristics of Basalts in Sanshui Basin and the Early Tectonic Evolution Stage of the South China Sea. *Mar. Geol. Quat. Geol.* **2021**, *41*, 95–113. [CrossRef]
70. Frey, F.A.; Green, D.H.; Roy, S.D. Integrated Models of Basalt Petrogenesis: A Study of Quartz Tholeiites to Olivine Melilitites from South Eastern Australia Utilizing Geochemical and Experimental Petrological Data. *J. Petrol.* **1978**, *19*, 463–513. [CrossRef]
71. Neave, D.A.; Fabbro, G.; Herd, R.A.; Petrone, C.M.; Edmonds, M. Melting, Differentiation and Degassing at the Pantelleria Volcano, Italy. *J. Petrol.* **2012**, *53*, 637–663. [CrossRef]
72. Marshall, A.S.; MacDonald, R.; Rogers, N.W.; Fitton, J.G.; Tindle, A.G.; Nejbert, K.; Hinton, R.W. Fractionation of Peralkaline Silicic Magmas: The Greater Olkaria Volcanic Complex, Kenya Rift Valley. *J. Petrol.* **2009**, *50*, 323–359. [CrossRef]
73. McKENZIE, D.; O'Nions, R.K. Partial melt distributions from inversion of rare Earth element concentrations. *J. Petrol.* **1991**, *32*, 1021–1091. [CrossRef]
74. Fujimaki, H.; Tatsumoto, M.; Aoki, K.-i. Partition coefficients of Hf, Zr, and REE between phenocrysts and groundmasses. *J. Geophys. Res.* **1984**, *89*, B662–B672. [CrossRef]
75. Rollinson, H.R. *Using Geochemical Data: Evaluation, Presentation, Interpretation*; Longman Scientific & Technical, John Wiley & Sons: London, UK, 1993; p. 352.
76. Foley, S.F.; Jackson, S.E.; Fryer, B.J.; Greenough, J.D.; Jenner, G.A. Trace element partition coefficients for clinopyroxene and phlogopite in an alkaline lamprophyre from Newfoundland by LAM-ICP-MS. *Geochim. Et Cosmochim. Acta* **1996**, *60*, 629–638. [CrossRef]
77. Mahood, G.A.; Stimac, J.A. Trace-element partitioning in pantellerites and trachytes. *Geochim. Et Cosmochim. Acta* **1990**, *54*, 2257–2276. [CrossRef]
78. Zack, T.; Brumm, R. Ilmenite/liquid partition coefficients of 26 trace elements determined through ilmenite/clinopyroxene partitioning in garnet pyroxene. In *7th International Kimberlite Conference*; Gurney, J.J., Gurney, J.L., Pascoe, M.D., Richardson, S.H., Eds.; Red Roof Design: Cape Town, South Africa, 1998; pp. 986–988.
79. Ewart, A.; Griffin, W.L. Application of proton-microprobe data to trace-element partitioning in volcanic rocks. *Chem. Geol.* **1994**, *117*, 251–284. [CrossRef]
80. Villemant, B. Trace-Element Evolution in the Phlegrean Fields (Central-Italy)—Fractional Crystallization and Selective Enrichment. *Contrib. Mineral. Petrol.* **1988**, *98*, 169–183. [CrossRef]